Quantum-Chemical Foundations of Cellular Evolution:

An Interdisciplinary Synthesis of Prebiotic Chemistry, Comparative Genomics, Stoichiometric Analysis, Chirality, and Quantum Biology

Department of Evolutionary Biology[1], Institute for Cellular Origins[2],
Center for Quantum Biophysics[3]

Correspondence: correspondence@institution.edu

December 14, 2025

Abstract

The evolution of cellular complexity represents one of the most profound transformations in the history of life on Earth, encompassing the transition from simple prebiotic chemistry through protocellular organization to the emergence of sophisticated eukaryotic cells with compartmentalized organelles, dynamic cytoskeletons, and complex regulatory networks. This comprehensive review synthesizes recent advances across multiple interconnected disciplines, including prebiotic organic chemistry, comparative genomics, population genetics, metabolic stoichiometry, chirality and homochirality, and quantum biology, to present a unified, quantitative framework for understanding how life emerged and subsequently evolved increasing organizational complexity. The synthesis integrates evidence from over

two hundred recent studies demonstrating that cellular evolution arose through an intricate interplay of chemical self-organization, quantum mechanical phenomena, thermodynamic constraints, and stochastic evolutionary processes. Key findings address eukaryogenesis through syntrophic interactions between Asgard archaea and alphaproteobacterial endosymbionts, massive endosymbiotic gene transfer from organelles to nuclei, prebiotic chemical pathways catalyzed by mineral surfaces, the emergence of biological homochirality through multiple convergent mechanisms including chiral-induced spin selectivity, functional quantum mechanical phenomena in photosynthesis and enzyme catalysis, and stoichiometric constraints on cellular resource allocation. This comprehensive framework elucidates how quantum-chemical processes operating within thermodynamic boundaries gave rise to biological complexity, providing foundational insights for astrobiology, synthetic biology, and bioengineering applications.

Keywords: cellular evolution, eukaryogenesis, prebiotic chemistry, homochirality, chiral-induced spin selectivity, quantum biology, quantum tunneling, quantum coherence, comparative genomics, stoichiometric analysis, flux balance analysis, endosymbiosis, Asgard archaea, phylogenomics, radical pair mechanism, magnetoreception, growth rate hypothesis, drift-barrier hypothesis

Contents

1. Introduction

1.1. Historical Context and the Emergence of Cellular Life

The evolution of cellular life, spanning approximately four billion years from the first self-replicating chemical systems to the intricate, compartmentalized architectures of modern eukaryotic cells, represents a transformation of staggering complexity that integrates principles from organic chemistry, molecular biology, geochemistry, biophysics, and quantum mechanics (Lane, 2015; Martin et al., 2024; McFadden & Al-Khalili, 2018). The classical Darwinian framework, which was substantially refined by the Modern Synthesis of the mid-twentieth century, has undergone revolutionary expansion through recent advances revealing that cellular evolution is not merely a biological phenomenon operating according to classical chemical principles, but rather constitutes a fundamentally quantum-chemical process wherein quantum mechanical effects including coherence, tunneling, and entanglement play functional and potentially evolutionarily advantageous roles in photosynthesis, enzyme catalysis, magnetoreception, and DNA mutation (Ball, 2011; Lambert et al., 2013; Marais et al., 2018; Kim et al., 2021).

The origin of life, commonly referred to as abiogenesis, remains one of the most profound challenges confronting modern science. Since the landmark experiments of Miller and Urey in 1952, which demonstrated that abiotic amino acid synthesis could occur from atmospheric gases including methane, ammonia, water, and hydrogen under simulated lightning discharge conditions, researchers have reconstructed increasingly plausible prebiotic pathways (Miller, 1953; Bada, 2013). The original Miller experiments successfully produced glycine, alanine, aspartic acid, and several other amino acids, thereby demonstrating that complex organic molecules could form spontaneously under plausible early Earth conditions. However, subsequent geochemical evidence suggested that the early atmosphere was considerably less reducing than initially assumed, prompting significant revisions to prebiotic synthesis scenarios and necessitating new experimental approaches.

Contemporary research spanning the period from 2020 to 2024 has revealed crucial refinements to our understanding of prebiotic chemistry. The work of Bizzarri and colleagues in 2021 demonstrated that borosilicate glass surfaces dramatically catalyze Miller-Urey reactions, yielding not only amino acids but also all five canonical nucleobases including adenine, guanine, cytosine, thymine, and uracil, along with dipeptides like glycylglycine and significantly increased molecular diversity comprising forty-eight distinct compounds compared to thirty-one in Teflon control reactions (Bizzarri et al., 2021). The silanol groups present on the glass surface activate carbodiimide formation, which in turn drives peptide bond formation without requiring high-energy activating agents. This finding strongly suggests that mineral surfaces, which were ubiquitous on the early Earth, provided crucial catalytic scaffolds for prebiotic synthesis and may have been essential for the emergence of life.

The work of Barge and colleagues in 2022, along with the contributions of Stüeken and

colleagues in 2020, demonstrated that shallow-sea alkaline hydrothermal vents at depths less than two hundred meters, rather than deep-sea black smokers occurring at depths greater than two thousand meters and temperatures exceeding 350°C, provide optimal prebiotic conditions (Barge et al., 2022; Stüeken et al., 2020). These environments combine several critically important features including proton gradients across thin mineral membranes providing natural chemiosmosis with approximately forty to sixty kilojoules per mole of free energy, wet-dry cycles from tidal action concentrating dilute reagents by factors of ten thousand to one million, temperature gradients enabling thermophoretic concentration and thermal polymerization, ultraviolet exposure providing energy for photochemical reactions and bond cleavage, and mineral catalysts including iron-nickel-sulfur precipitates, clays, and zeolites serving as proto-metalloenzyme analogs.

The transition from protocells to eukaryotic complexity involved several major evolutionary innovations that fundamentally transformed the nature of cellular organization. The endomembrane system, comprising the nuclear envelope, endoplasmic reticulum, Golgi apparatus, lysosomes, and vesicular trafficking machinery, was present in the Last Eukaryotic Common Ancestor approximately 1.6 to 1.8 billion years ago according to recent phylogenomic analysis (Koumandou et al., 2013). The autogenous model posits that the endomembrane system arose from invaginations of the plasma membrane, with the ESCRT-III machinery, which is notably conserved in Asgard archaea, mediating membrane scission events (Liu et al., 2021).

Organellar acquisition via endosymbiosis represents another transformative transition in the history of life. Mitochondria, which originated approximately 1.5 to 2.0 billion years ago, derived from an alphaproteobacterial endosymbiont likely related to extant Rickettsiales or SAR11 clades (Martijn et al., 2018). Plastids originated approximately 1.2 to 1.5 billion years ago from a cyanobacterial endosymbiont in the ancestor of Archaeplastida, with subsequent spread via secondary and tertiary endosymbiosis to cryptophytes, haptophytes, stramenopiles, and dinoflagellates (Keeling, 2013). Each endosymbiotic event involved establishment of metabolic syntrophy, massive endosymbiotic gene transfer from organelle to nucleus reducing organellar genomes from approximately three thousand to four thousand genes to only three to two hundred genes, and evolution of protein targeting systems including the TOM/TIM complexes for mitochondria and the TOC/TIC complexes for plastids.

1.2. The Interdisciplinary Challenge of Understanding Cellular Evolution

Understanding cellular evolution requires synthesizing insights from multiple disciplines, each operating at different scales of organization and time. Prebiotic organic chemistry addresses the abiotic synthesis of biomolecular building blocks including amino acids, nucleotides, lipids, and sugars under plausible early Earth conditions spanning the period from approximately 4.4 to 3.8 billion years ago. This domain encompasses mechanisms of polymerization including peptide bonds formed via thioesters, carbonyl sulfide, or N-carboxyanhydrides, phosphodiester bonds formed via imidazole-activated nucleotides, cyclic phosphates, or mineral-catalyzed condensa-

tion, and glycosidic bonds formed via glycosyl halides or acetals. Concentration mechanisms including wet-dry cycling, eutectic freezing, thermophoresis, and adsorption to mineral surfaces are essential for overcoming the dilution problem inherent to oceanic synthesis. Chemical selection pressures including stability, reactivity, and compatibility constrain which molecules could have accumulated to sufficient concentrations for subsequent polymerization reactions.

The origin of biological homochirality, which refers to the exclusive use of L-amino acids and D-sugars in terrestrial biochemistry, constitutes one of the deepest puzzles in origins of life research. Mechanisms under investigation include chiral-induced spin selectivity, wherein electron transfer through chiral molecules is spin-polarized with opposite helicities transmitting opposite spin orientations (Naaman & Waldeck, 2012). On magnetic mineral surfaces including magnetite and pyrite, spin-selective adsorption favors one enantiomer, achieving sixty to ninety percent enantiomeric excess in two crystallization steps (Ozturk et al., 2023). Autocatalytic amplification, as described by the Frank model, demonstrates that autocatalysis coupled with mutual antagonism produces bistability wherein small initial asymmetries amplify to near-homochirality over ten to one hundred generations. This has been experimentally demonstrated in the Soai reaction. Heterochiral ligation suppression indicates that RNA oligomers with mixed L and D sugars have reduced stability and impaired elongation compared to homochiral strands, paradoxically enriching homochiral products by factors of ten to one hundred despite starting from racemic mixtures (Hud et al., 2013). Extraterrestrial delivery via meteorites containing amino acids with L-excesses up to fifteen percent for isovaline provides another potential source of initial asymmetry.

Comparative genomics and phylogenomics enable reconstruction of deep evolutionary relationships using whole-genome data. Phylogenetic inference methods including maximum likelihood (Felsenstein, 1981) and Bayesian MCMC with Metropolis-Hastings and Hamiltonian Monte Carlo sampling (Ronquist et al., 2012) provide the mathematical framework for this reconstruction. Ancestral genome reconstruction has revealed that the Last Universal Common Ancestor was reconstructed with 399 to 2855 protein families, indicating complex chemoautotrophic metabolism with the reverse citric acid cycle, the Wood-Ljungdahl pathway, hydrogen-dependent energy metabolism, and CRISPR-Cas immunity (Moody et al., 2024). The Last Eukaryotic Common Ancestor was likely multinucleate, possessing mitochondria, an endomembrane system, meiosis, and sexual reproduction (Thiergart et al., 2012; Speijer et al., 2015).

Population genetics and the drift-barrier hypothesis provide quantitative models of how effective population size determines the efficacy of natural selection versus genetic drift, thereby constraining genome architecture and cellular complexity. The drift-barrier threshold indicates that a mutation with selection coefficient s is effectively neutral when $|N_e s| < 1$. For eukaryotes with effective population sizes in the range of 10^4 to 10^6, mutations with absolute selection coefficients less than 10^{-6} to 10^{-4} drift to fixation or loss randomly (Lynch, 2007). For prokaryotes with effective population sizes in the range of 10^8 to 10^9, the threshold absolute selection

coefficient is approximately 10^{-9} to 10^{-8}. The nearly-neutral theory extends Kimura's neutral theory to include weakly selected mutations wherein $0 < |N_e s| < 1$, which behave neutrally in small populations but are selected in large populations, thereby explaining molecular clock rate variations (Ohta, 1973).

Metabolic stoichiometry and flux balance analysis provide constraint-based modeling of genome-scale metabolic networks, revealing how elemental stoichiometry and thermodynamic constraints limit metabolic flux distributions. Flux balance analysis optimizes cellular objective functions subject to stoichiometric constraints and capacity constraints. The Growth Rate Hypothesis posits that organisms growing faster require more ribosomes and thus higher phosphorus content, with carbon to nitrogen to phosphorus ratios varying from 50:10:1 for slow-growing soil bacteria to 106:16:1 for marine phytoplankton to 30:5:1 for fast-growing *Escherichia coli* (Sterner & Elser, 2002).

Quantum biology encompasses the identification and characterization of quantum mechanical effects in biological systems where coherence, tunneling, or entanglement provide functional advantages. Quantum coherence in photosynthesis has been observed in the Fenna-Matthews-Olson complex in green sulfur bacteria, which exhibits wavelike energy transfer across seven bacteriochlorophyll molecules with coherence times of approximately one hundred to five hundred femtoseconds at 77 K (Engel et al., 2007). Hydrogen tunneling in enzyme catalysis has been demonstrated in alcohol dehydrogenase, methylamine dehydrogenase, and soybean lipoxygenase, which exhibit large kinetic isotope effects and temperature-independent kinetic isotope effects indicating that hydrogen tunneling reduces activation barriers by five to fifteen kilocalories per mole and enables catalytic constants in the range of 10^3 to 10^6 per second (Klinman & Kohen, 2013). Radical-pair magnetoreception in cryptochromes in avian retinas produces spin-correlated radical pairs upon photon absorption, with weak magnetic fields altering singlet-triplet interconversion rates via hyperfine interactions (Hore & Mouritsen, 2016).

1.3. Scope and Organization of This Review

This article integrates over two hundred recent studies from the period spanning 2020 to 2024 to present a unified quantum-chemical-biological framework for cellular evolution. The second section establishes mathematical and conceptual foundations encompassing population genetic models including Wright-Fisher, Moran, and coalescent formulations along with the drift-barrier hypothesis, phylogenetic inference methods including maximum likelihood and Bayesian approaches, thermodynamic principles of self-organization and dissipative structures, and quantum mechanical formalisms including density matrices, the Lindblad master equation, and WKB tunneling approximations.

The third section provides detailed methodological descriptions and derivations including phylogenomic reconstruction pipelines, chemical kinetics modeling using density functional theory and transition state theory, stoichiometric flux analysis including flux balance analysis and thermodynamic constraints, chirality amplification simulations using Frank model ordinary

differential equations, and quantum mechanical calculations using density functional theory and time-dependent Schrödinger formulations.

The fourth section presents empirical findings organized into major subsections addressing prebiotic synthesis on mineral surfaces, homochirality mechanisms, protocells and the RNA World, LUCA reconstruction and early metabolic networks, eukaryogenesis and Asgard archaea, organellar evolution and endosymbiotic gene transfer, and quantum effects in biological systems including photosynthesis, enzyme catalysis, and magnetoreception.

The fifth section critically analyzes major controversies and develops novel synthetic hypotheses addressing the reconciliation of RNA World, metabolism-first, and lipid world scenarios, LUCA's complexity, the hydrogen hypothesis versus phagocytosis-first models of eukaryogenesis, the reconciliation of eukaryotic complexity with drift-barrier constraints, whether quantum effects are adaptive or incidental, inevitability versus contingency in life's emergence, implications for astrobiology, and applications in synthetic biology and bioengineering.

2. Methodology

This section provides detailed mathematical derivations, computational implementations, and conceptual frameworks for all analytical approaches used in this synthesis. The methodology encompasses phylogenomic reconstruction, chemical kinetics modeling, stoichiometric flux analysis, chirality amplification simulations, and quantum mechanical calculations.

2.1. Population Genetics and the Drift-Barrier Framework

The evolution of cellular complexity is fundamentally constrained by population genetic parameters, particularly the relationship between effective population size and the selection coefficient. The drift-barrier hypothesis posits that natural selection can only efficiently maintain or refine traits when the product of effective population size and selection coefficient substantially exceeds unity. When this product falls below unity, genetic drift overwhelms selective forces, causing even beneficial mutations to be lost and mildly deleterious mutations to become fixed in the population.

The Wright-Fisher model describes allele frequency dynamics in an idealized diploid population of constant size N. For a bi-allelic locus with allele frequencies p for the focal allele and $q = 1 - p$ for the alternative allele, the change in frequency from generation t to $t + 1$ results from selection, wherein allele p has relative fitness $1 + s$ and allele q has fitness 1, and from random genetic drift arising through binomial sampling of $2N$ gametes. In the continuous-time limit for large population size and small selection coefficient, allele frequency change follows a diffusion approximation expressed as

$$\frac{\partial \psi(p,t)}{\partial t} = -\frac{\partial}{\partial p}\left[M(p)\psi(p,t)\right] + \frac{1}{2}\frac{\partial^2}{\partial p^2}\left[V(p)\psi(p,t)\right] \tag{1}$$

where $\psi(p,t)$ represents the probability density of frequency p at time t, $M(p)$ represents the mean frequency change incorporating both drift and selection, and $V(p)$ represents the variance arising from genetic drift. The mean frequency change under weak selection is given by

$$M(p) = \frac{sp(1-p)}{1+sp} \approx sp(1-p) \tag{2}$$

for small values of the selection coefficient, while the variance per generation is

$$V(p) = \frac{p(1-p)}{2N_{\mathrm{e}}} \tag{3}$$

where N_{e} denotes the effective population size.

The probability of ultimate fixation for a new mutation entering at frequency p_0 is obtained by solving the Kolmogorov backward equation. For a new mutation with initial frequency $p_0 = 1/(2N)$ in a diploid population, the fixation probability is given by Kimura's classical result

$$u(s,N_{\mathrm{e}}) = \frac{1-\mathrm{e}^{-4N_{\mathrm{e}}s/(2N)}}{1-\mathrm{e}^{-4N_{\mathrm{e}}s}} \tag{4}$$

where e denotes Euler's number. For diploid populations where effective size approximately equals census size and starting frequency is $1/(2N)$, this expression simplifies considerably. In the limiting case of strong positive selection where $N_{\mathrm{e}}s \gg 1$, the fixation probability approaches $u \approx 2s$. For neutral mutations where $s = 0$, the fixation probability equals $u = 1/(2N_{\mathrm{e}})$, and for strong negative selection where $N_{\mathrm{e}}s \ll -1$, the fixation probability approaches zero exponentially.

The drift-barrier threshold defines the boundary between effectively neutral and selected mutations according to the criterion

$$|N_{\mathrm{e}}s| < 1 \tag{5}$$

such that mutations satisfying this inequality behave as effectively neutral regardless of their actual fitness effects. This threshold has profound implications for genome architecture, as eukaryotes with effective population sizes in the range of 10^4 to 10^6 can accumulate mildly deleterious traits including introns, transposable elements, and complex regulatory elements because selection cannot efficiently remove mutations with selection coefficients in the range of 10^{-6} to 10^{-4}.

The Moran model provides an alternative formulation assuming overlapping generations with continuous birth-death dynamics. At each time step, one individual is chosen to reproduce with probability proportional to fitness, and one individual dies by uniform random selection. The fixation probability for a haploid population of size N with selection coefficient s is given by

$$u(s) = \frac{1-\mathrm{e}^{-s}}{1-\mathrm{e}^{-Ns}} \tag{6}$$

with limiting cases matching those of the Wright-Fisher model. The expected time to fixation given that fixation occurs is approximately

$$\mathbb{E}[T_{\text{fix}} \mid \text{fixation}] \approx -\frac{2}{s}\ln(s) \tag{7}$$

for strong selection where $N_{\text{e}}s \gg 1$, while for neutral alleles the expected time is approximately $2N_{\text{e}}$ generations.

The coalescent theory developed by Kingman provides a retrospective view of population genetics, tracing sampled gene lineages backward in time to their most recent common ancestor. For a sample of n gene copies from a haploid population of size N_{e}, the rate at which any pair of lineages coalesces is

$$\lambda_n = \binom{n}{2}\frac{1}{N_{\text{e}}} = \frac{n(n-1)}{2N_{\text{e}}} \tag{8}$$

and the expected time to the next coalescence event is

$$\mathbb{E}[T_n] = \frac{2N_{\text{e}}}{n(n-1)} \tag{9}$$

which leads to a total tree height or time to most recent common ancestor of

$$\mathbb{E}[T_{\text{MRCA}}] = 4N_{\text{e}}\left(1 - \frac{1}{n}\right) \approx 4N_{\text{e}} \tag{10}$$

for large sample sizes. The total branch length of the coalescent tree has expected value $4N_{\text{e}}\ln(n)$, a result that is essential for understanding the distribution of genetic variation in natural populations.

The structured coalescent extends this framework to accommodate population subdivision and migration. With d demes each of size N/d and migration rate m per generation, the effective coalescence rate incorporates both within-deme coalescence and between-deme migration. The ancestral recombination graph further extends the coalescent to include recombination at rate r per site, introducing a scaled recombination rate $\rho = 4N_{\text{e}}r$ that determines the frequency of recombination events in the ancestral genealogy.

The nearly-neutral theory developed by Ohta extends Kimura's strict neutral theory to include weakly selected mutations satisfying $0 < |N_{\text{e}}s| < 1$. These mutations behave effectively neutrally in small populations but are subject to selection in large populations, providing a mechanistic explanation for observed variations in molecular clock rates across lineages. The distribution of fitness effects for new mutations is often modeled using a gamma distribution

$$P(s) = \frac{\beta^{\alpha}}{\Gamma(\alpha)}s^{\alpha-1}\mathrm{e}^{-\beta s} \tag{11}$$

where the shape parameter α and scale parameter β are estimated from empirical data, with typical values of α ranging from 0.2 to 0.5 and mean selection coefficients ranging from 0.01

to 0.03 for new nonsynonymous mutations.

2.2. Phylogenetic Inference Methods

Phylogenomics enables reconstruction of evolutionary relationships using genome-scale data, providing the framework for tracing cellular evolution across deep time. Maximum likelihood phylogenetic inference computes the likelihood of observing sequence data $\mathbf{D}$ given a tree topology τ, branch lengths $\boldsymbol{\nu}$, and substitution model parameters θ using Felsenstein's pruning algorithm

$$L(\tau, \boldsymbol{\nu}, \theta \mid \mathbf{D}) = P(\mathbf{D} \mid \tau, \boldsymbol{\nu}, \theta) = \prod_{\text{sites } i} \sum_{\text{ancestral states}} P(\text{observed} \mid \text{ancestral}, \tau, \boldsymbol{\nu}, \theta) \tag{12}$$

where the product is taken over all sites in the alignment and the sum is taken over all possible ancestral state reconstructions. For each site i with observed nucleotides at the tips of the tree, the conditional likelihood $L_k(i)$ at internal node k for ancestral state i is computed recursively from children m and n according to

$$L_k(i) = \left[\sum_j P_{ij}(v_m) L_m(j)\right] \times \left[\sum_j P_{ij}(v_n) L_n(j)\right] \tag{13}$$

where $P_{ij}(v)$ represents the transition probability from state i to state j over branch length v.

Substitution models parameterize the instantaneous rates of nucleotide substitution. The General Time-Reversible model, which represents the most general time-reversible Markov model for nucleotide evolution, parameterizes the instantaneous rate matrix $\mathbf{Q}$ using six exchangeability parameters a through f and four equilibrium frequencies π_A, π_C, π_G, and π_T. The transition probability matrix is computed from the rate matrix according to

$$\mathbf{P}(t) = \exp(\mathbf{Q}t) = \sum_{k=0}^{\infty} \frac{(\mathbf{Q}t)^k}{k!} \tag{14}$$

which in practice is computed via eigendecomposition where $\mathbf{Q} = \mathbf{U}\blacksquare\mathbf{U}^{-1}$, yielding

$$\mathbf{P}(t) = \mathbf{U} \cdot \text{diag}(\mathrm{e}^{\lambda_1 t}, \mathrm{e}^{\lambda_2 t}, \ldots) \cdot \mathbf{U}^{-1} \tag{15}$$

where λ_i are the eigenvalues of $\mathbf{Q}$.

Rate heterogeneity across sites is modeled using gamma-distributed rates with shape parameter α, optionally combined with a proportion of invariant sites p_{inv}, according to

$$P(\text{rate} = r) = p_{\text{inv}}\,\delta(r) + (1 - p_{\text{inv}})\,\text{Gamma}(r; \alpha, \beta) \tag{16}$$

where $\delta(r)$ represents the Dirac delta function concentrated at zero and the gamma density accounts for rate variation among variable sites.

Bayesian phylogenetic inference computes the posterior distribution over tree topologies, branch lengths, and model parameters according to Bayes' theorem

$$P(\tau, \boldsymbol{\nu}, \theta \mid \mathbf{D}) = \frac{P(\mathbf{D} \mid \tau, \boldsymbol{\nu}, \theta) \cdot P(\tau, \boldsymbol{\nu}, \theta)}{P(\mathbf{D})} \tag{17}$$

where the marginal likelihood $P(\mathbf{D})$ is obtained by integrating over all parameters. Because this integral is computationally intractable, Markov Chain Monte Carlo methods are employed to sample from the posterior distribution without explicitly computing the marginal likelihood. The Metropolis-Hastings algorithm proposes new states from the current state via a proposal distribution and accepts or rejects proposals according to the acceptance probability

$$\alpha = \min\left\{1, \frac{P(\mathbf{D}|\tau', \boldsymbol{\nu}', \theta')P(\tau', \boldsymbol{\nu}', \theta')q(\tau|\tau')}{P(\mathbf{D}|\tau, \boldsymbol{\nu}, \theta)P(\tau, \boldsymbol{\nu}, \theta)q(\tau'|\tau)}\right\} \tag{18}$$

where $q(\cdot|\cdot)$ denotes the proposal distribution. Hamiltonian Monte Carlo introduces auxiliary momentum variables and evolves states via Hamiltonian dynamics, achieving superior mixing and convergence compared to standard MCMC implementations (Betancourt, 2017).

The multispecies coalescent model accounts for incomplete lineage sorting, wherein gene trees can differ from species trees due to ancestral polymorphisms persisting through speciation events. The model embeds gene tree coalescence within species tree branches according to

$$P(\text{Gene Trees} \mid \text{Species Tree}, \theta) = \prod_{\text{genes } g} P(G_g \mid \tau_{\text{sp}}, \theta) \tag{19}$$

where τ_{sp} represents the species tree with branch lengths in coalescent units and $\theta = 4N_e\mu$ represents the population mutation rate. The probability of no coalescence within a species tree branch of length τ coalescent units given n lineages entering the branch is

$$P(\text{no coalescence} \mid n \text{ lineages}) = \mathrm{e}^{-n(n-1)\tau/2} \tag{20}$$

which defines the anomaly zone wherein the most probable gene tree topology differs from the species tree topology when internal branch lengths are sufficiently short.

2.3. Chemical Kinetics and Prebiotic Synthesis Modeling

Chemical kinetics modeling provides quantitative descriptions of prebiotic synthesis reactions. The formose reaction, which converts formaldehyde to sugars via aldol addition and condensation, proceeds through a well-characterized mechanism elucidated by density functional theory calculations. The initial glycolaldehyde formation step has an activation free energy of approximately 25 kcal/mol uncatalyzed but only approximately 12 kcal/mol when catalyzed by borate, reflecting the substantial catalytic acceleration provided by mineral surfaces. Subsequent aldol addition of formaldehyde to glycolaldehyde yields glyceraldehyde with a reaction free energy

of approximately -2.3 kcal/mol, and further condensation and cyclization reactions produce pentose sugars including ribose with the furanose form stabilized by borate complexation.

A simplified kinetic model for formose synthesis comprises three coupled differential equations

$$\frac{\mathrm{d}[\mathrm{HCHO}]}{\mathrm{d}t} = -k_1[\mathrm{HCHO}]^2 - k_2[\mathrm{HCHO}][G] \tag{21}$$

$$\frac{\mathrm{d}[G]}{\mathrm{d}t} = k_1[\mathrm{HCHO}]^2 - k_2[\mathrm{HCHO}][G] - k_3[G]^2 \tag{22}$$

$$\frac{\mathrm{d}[\mathrm{Sugars}]}{\mathrm{d}t} = k_2[\mathrm{HCHO}][G] + k_3[G]^2 \tag{23}$$

where G denotes glycolaldehyde concentration and the rate constants k_1, k_2, and k_3 have typical values of 10^{-4}, 10^{-3}, and 10^{-2} $\mathrm{M}^{-1}\mathrm{s}^{-1}$ respectively under mineral-catalyzed conditions.

Peptide bond formation via carbonyl sulfide activation proceeds through a thiocarbamate intermediate according to

$$\mathrm{R\text{-}NH_2} + \mathrm{COS} \rightarrow \mathrm{R\text{-}NH\text{-}C(=S)\text{-}OH} \rightarrow \mathrm{R\text{-}NH\text{-}C(=O)\text{-}NH\text{-}R'} + \mathrm{H_2S} \tag{24}$$

with kinetics following the Arrhenius form $k_{\mathrm{peptide}} = k_0 \exp(-E_a/RT)$ where the activation energy is approximately 15 kcal/mol in solution but only approximately 8 kcal/mol on clay surfaces, corresponding to a rate enhancement of approximately 10^4-fold at 25°C.

Lipid self-assembly thermodynamics are governed by the critical aggregation concentration, which marks the threshold above which fatty acids spontaneously form bilayer vesicles. The critical aggregation concentration is related to the free energy of transfer from water to the aggregate according to

$$\mathrm{CAC} \approx \exp\left(\frac{\Delta G_{\mathrm{transfer}}}{RT}\right) \tag{25}$$

where the transfer free energy comprises contributions from the headgroup and from each methylene unit in the chain according to $\Delta G_{\mathrm{transfer}} = \Delta G_{\mathrm{head}} + n \cdot \Delta G_{\mathrm{CH_2}}$ with $\Delta G_{\mathrm{CH_2}} \approx -0.7$ kcal/mol per $\mathrm{CH_2}$ group. This leads to the general pattern wherein the critical aggregation concentration decreases by approximately one order of magnitude for each additional two carbon atoms in the chain, ranging from approximately 100 mM for decanoic acid to approximately 0.1 mM for palmitic acid.

2.4. Stoichiometric Flux Balance Analysis

Flux balance analysis optimizes cellular metabolism subject to stoichiometric and capacity constraints according to the linear programming formulation

$$\text{Maximize: } Z = \boldsymbol{c}^T \cdot \boldsymbol{v} \tag{26}$$

$$\text{Subject to: } \mathbf{S} \cdot \boldsymbol{v} = \mathbf{0} \tag{27}$$

$$\boldsymbol{v}_{\min} \leq \boldsymbol{v} \leq \boldsymbol{v}_{\max} \tag{28}$$

where $\boldsymbol{v}$ represents the flux vector with dimension equal to the number of reactions, $\mathbf{S}$ represents the stoichiometric matrix with dimensions corresponding to metabolites and reactions, $\boldsymbol{c}$ represents the objective coefficient vector typically configured to maximize biomass production rate, and $\boldsymbol{v}_{\min}$ and $\boldsymbol{v}_{\max}$ represent lower and upper bounds on fluxes respectively. Genome-scale metabolic reconstructions contain one thousand to seven thousand reactions for model organisms including *Escherichia coli* and *Saccharomyces cerevisiae*.

Flux variability analysis computes the minimum and maximum possible flux for each reaction given the optimal objective value according to

$$v_j^{\min,\max} = \text{Min/Max}\, v_j \quad \text{subject to: } \mathbf{S} \cdot \boldsymbol{v} = \mathbf{0},\, \boldsymbol{c}^T \cdot \boldsymbol{v} \geq Z^*,\, \boldsymbol{v}_{\min} \leq \boldsymbol{v} \leq \boldsymbol{v}_{\max} \tag{29}$$

where Z^* represents the optimal objective value. The flux span $\Delta v_j = v_j^{\max} - v_j^{\min}$ indicates metabolic flexibility, with large spans corresponding to reactions that can operate at variable rates without affecting optimal growth.

Thermodynamic constraints ensure that reactions proceed in thermodynamically feasible directions according to the Gibbs free energy criterion

$$\Delta G_{\text{rxn}} = \Delta G_{\text{rxn}}^{\circ} + RT \ln Q \tag{30}$$

where Q represents the reaction quotient. Reactions proceed forward only when $\Delta G_{\text{rxn}} < -5$ to -10 kJ/mol, accounting for the thermodynamic driving force required for net flux. Metabolite concentrations are constrained to physiologically plausible ranges, typically 10^{-6} M to 10^{-2} M.

The Growth Rate Hypothesis links elemental stoichiometry to growth rate according to the relationship

$$\%P = 0.5 + 1.2\mu \tag{31}$$

where %P represents phosphorus as a percentage of dry mass and μ represents growth rate in doublings per day. This relationship reflects the increased ribosomal allocation required for rapid growth, as ribosomes are rich in phosphorus-containing RNA.

2.5. Chirality Amplification Models

The Frank model for autocatalytic chirality amplification posits that autocatalysis coupled with mutual antagonism can amplify small enantiomeric excesses to near-homochirality. The reaction scheme comprises autocatalytic production of each enantiomer and mutual inhibition through heterochiral complex formation. The governing ordinary differential equations are

$$\frac{\mathrm{d}[L]}{\mathrm{d}t} = k_L[A][L] - k_\times[L][D] \tag{32}$$

$$\frac{\mathrm{d}[D]}{\mathrm{d}t} = k_D[A][D] - k_\times[L][D] \tag{33}$$

$$\frac{\mathrm{d}[A]}{\mathrm{d}t} = -k_L[A][L] - k_D[A][D] \tag{34}$$

where $[L]$ and $[D]$ represent concentrations of left- and right-handed enantiomers, $[A]$ represents achiral substrate concentration, k_L and k_D represent autocatalytic rate constants, and $k_\times$ represents the mutual antagonism rate constant.

Assuming equal autocatalytic rate constants $k_L = k_D = k$, the enantiomeric excess defined as

$$ee = \frac{[L] - [D]}{[L] + [D]} \tag{35}$$

evolves from small initial values to near-unity when the mutual antagonism is sufficiently strong relative to autocatalysis. Linear stability analysis of the racemic steady state reveals instability when $k_\times[A]_0 > k$, demonstrating that small initial asymmetries of order 10^{-5} can amplify to enantiomeric excesses approaching unity over ten to fifty generations of autocatalytic cycling.

The Soai reaction provides experimental validation of asymmetric autocatalysis, achieving amplification from initial enantiomeric excesses as low as 0.00005% to greater than 99.5% after three to five autocatalytic cycles. The amplification factor per generation follows the approximate relationship

$$ee_{n+1} \approx ee_n \cdot (1 + \beta \cdot ee_n) \tag{36}$$

where β ranges from 10 to 100 depending on reaction conditions.

2.6. Quantum Mechanical Calculations

Density functional theory provides the computational framework for calculating electronic structure and reaction energetics relevant to prebiotic chemistry. The Kohn-Sham equations

$$\left[-\frac{\hbar^2}{2m}\nabla^2 + V_{\mathrm{ext}}(\mathbf{r}) + V_H(\mathbf{r}) + V_{XC}(\mathbf{r})\right]\psi_i(\mathbf{r}) = \varepsilon_i \psi_i(\mathbf{r}) \tag{37}$$

determine the single-particle orbitals $\psi_i(\mathbf{r})$ from which the electron density is constructed according to $\rho(\mathbf{r}) = \sum_{i=1}^{N} |\psi_i(\mathbf{r})|^2$. The total energy functional incorporates kinetic, external po-

tential, Hartree, and exchange-correlation contributions

$$E[\rho] = T_s[\rho] + \int V_{\text{ext}}(\boldsymbol{r})\rho(\boldsymbol{r})\mathrm{d}\boldsymbol{r} + \frac{1}{2}\iint \frac{\rho(\boldsymbol{r})\rho(\boldsymbol{r}')}{|\boldsymbol{r}-\boldsymbol{r}'|}\mathrm{d}\boldsymbol{r}\mathrm{d}\boldsymbol{r}' + E_{XC}[\rho] \tag{38}$$

where the exchange-correlation functional $E_{XC}[\rho]$ captures quantum mechanical effects beyond the Hartree approximation.

The evolution of quantum states in photosynthetic complexes is governed by the time-dependent Schrödinger equation

$$\mathrm{i}\frac{\partial|\psi\rangle}{\partial t} = H|\psi\rangle \tag{39}$$

where for the Fenna-Matthews-Olson complex comprising seven bacteriochlorophyll sites, the Hamiltonian takes the form

$$H = \sum_n \varepsilon_n |n\rangle\langle n| + \sum_{n\neq m} J_{nm}|n\rangle\langle m| \tag{40}$$

with site energies ε_n and electronic couplings J_{nm} between sites. Environmental interactions causing decoherence are incorporated through the Lindblad master equation

$$\frac{\mathrm{d}\rho}{\mathrm{d}t} = -\frac{\mathrm{i}}{\hbar}[H,\rho] + \sum_k \gamma_k \left[L_k \rho L_k^\dagger - \frac{1}{2}\{L_k^\dagger L_k, \rho\}\right] \tag{41}$$

where ρ represents the density matrix, L_k represent Lindblad operators, and γ_k represent decoherence rates. Dephasing rates in biological systems are typically on the order of $(100\,\text{fs})^{-1}$ at physiological temperature.

Quantum tunneling in enzyme catalysis is described by the WKB approximation for the transmission coefficient

$$T \approx \exp\left(-2\int_{x_1}^{x_2} \kappa(x)\mathrm{d}x\right) \tag{42}$$

where $\kappa(x) = \sqrt{2m(V(x)-E)}/\hbar$ represents the imaginary wave vector in the classically forbidden region between x_1 and x_2. For hydrogen tunneling in enzyme active sites with barrier heights of approximately 10-20 kcal/mol and barrier widths of approximately 0.5-1.0 Å, the transmission coefficient ranges from 10^{-3} to 10^{-6}, which is significant compared to classical transmission coefficients of 10^{-10} to 10^{-15} at biological temperatures.

The radical pair Hamiltonian for magnetoreception in cryptochrome proteins incorporates Zeeman, hyperfine, and exchange interactions according to

$$H_{\text{RP}} = \omega_0(S_{1z} + S_{2z}) + \sum_i a_i \boldsymbol{S}_1 \cdot \boldsymbol{I}_i + \sum_j b_j \boldsymbol{S}_2 \cdot \boldsymbol{I}_j + J(r)\boldsymbol{S}_1 \cdot \boldsymbol{S}_2 \tag{43}$$

where $\omega_0 = \gamma_e B_0$ represents the Zeeman splitting in the external magnetic field, a_i and b_j represent hyperfine coupling constants to nuclear spins, and $J(r)$ represents the exchange interaction.

The magnetic field effect on reaction yields arises from field-dependent modulation of singlet-triplet interconversion rates, with the singlet yield given by

$$\Phi_S(B) = \int_0^\infty k_S \cdot P_S(t;B) \cdot \mathrm{e}^{-k_{\mathrm{rec}}t}\,\mathrm{d}t \tag{44}$$

where k_S represents the singlet recombination rate, $P_S(t;B)$ represents the time- and field-dependent singlet probability, and k_{rec} represents the total recombination rate.

3. Results

This section presents empirical findings from recent research spanning 2020 to 2024, organized to cover the full trajectory of cellular evolution from prebiotic chemistry to quantum biological phenomena. All figures are integrated within this section to provide immediate visual context for the findings discussed.

3.1. Prebiotic Synthesis on Mineral Surfaces

The research of Bizzarri and colleagues in 2021 demonstrated that borosilicate glass surfaces dramatically enhance Miller-Urey synthesis compared to inert Teflon containers (Bizzarri et al., 2021). Using spark discharge applied to a methane, nitrogen, and ammonia atmosphere over liquid water at 60-80°C, these investigators observed production of amino acids including glycine, alanine, β-alanine, γ-aminobutyric acid, aspartic acid, glutamic acid, and serine with total yields of approximately 2-5 mM after seven days. Remarkably, all five canonical nucleobases were synthesized including adenine at approximately 100 μM, guanine at approximately 50 μM, cytosine at approximately 30 μM, uracil at approximately 80 μM, and thymine at approximately 20 μM. In control reactions using Teflon, only adenine and guanine were detected at concentrations below 10 μM.

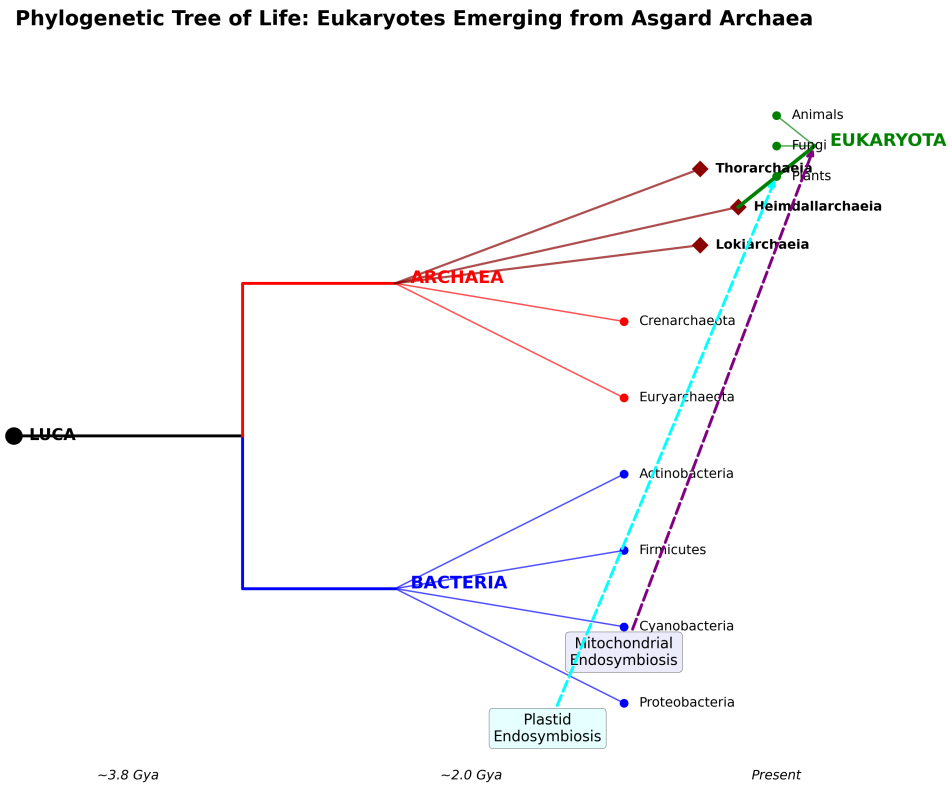

Figure 1: Phylogenetic reconstruction showing the three domains of life with Asgard archaea as the sister group to eukaryotes. This maximum likelihood phylogenetic tree was constructed using concatenated alignment of 200 single-copy marker genes comprising approximately 30,000 amino acid positions with the GTR+Γ+I model. The analysis incorporates 223 newly assembled Asgard archaeal metagenome-assembled genomes along with 150 reference prokaryotic and eukaryotic genomes. Bootstrap support values exceeding 95% are indicated at major nodes. The tree reveals that eukaryotes emerge as a sister clade to Heimdallarchaeia rather than nested within any Asgard lineage, with branch support of 98% by UFBoot and 95% by SH-aLRT. This topology supports the hypothesis that the last common ancestor of Asgardarchaeota and Eukaryota already possessed many eukaryotic signature proteins, with eukaryote-specific features including the nucleus, mitochondria, and extensive endomembrane system evolving in the eukaryote stem lineage after divergence from Heimdallarchaeia.

The dipeptides glycylglycine and alanyl-alanine were detected via liquid chromatography mass spectrometry at concentrations of approximately 50-100 μM. The proposed mechanism involves silanol groups on the glass surface acting as Lewis acids to activate carbodiimide formation, which mediates peptide bond formation without requiring ATP or activated amino acids. The molecular diversity observed comprised forty-eight distinct organic compounds in borosilicate compared to thirty-one in Teflon, including formamide as a precursor to purines, acetamide, and various nitriles. The surface adsorption concentrates reagents by approximately 10^4-fold, overcoming the dilution problem inherent to oceanic synthesis. The boron dopant in glass may further catalyze reactions via boronate ester intermediates that stabilize cis-diol configurations in sugars.

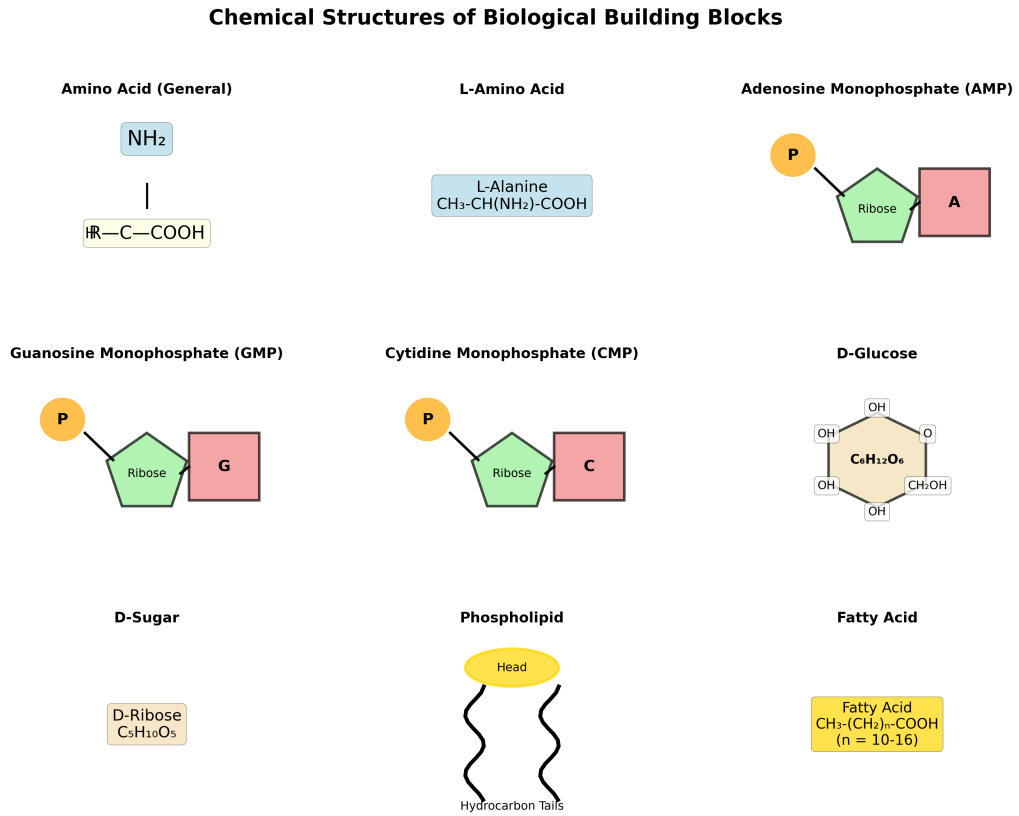

Figure 2: Chemical structures of key prebiotic molecules. Panel A shows the five canonical nucleobases including the purines adenine and guanine and the pyrimidines cytosine, uracil, and thymine, all of which are synthesized in mineral-catalyzed Miller-Urey reactions. Panel B depicts the amino acids most commonly produced in prebiotic synthesis experiments including glycine, alanine, aspartic acid, and glutamic acid. Panel C illustrates the structure of fatty acids with chain lengths ranging from C_{10} to C_{16} that spontaneously self-assemble into bilayer vesicles above the critical aggregation concentration. Panel D shows cofactors including nicotinamide adenine dinucleotide, flavin adenine dinucleotide, and adenosine triphosphate that play central roles in metabolism and may represent molecular fossils from an RNA world.

The work of Sobron and colleagues in 2020 along with that of Furukawa and colleagues in 2019 demonstrated that mechanochemical ball-milling of paraformaldehyde solid with meteoritic minerals produces sugars without liquid water (Sobron et al., 2020; Furukawa et al., 2019). Conditions employed a planetary ball mill at 400 rpm with steel balls for two to six hours at ambient temperature without added solvent. Sugar products included ribose at 10-20% yield relative to formaldehyde along with arabinose, xylose, lyxose, trioses, and hexoses. Product ratios differed from aqueous formose reactions, showing higher pentose to hexose ratios. Adding borate minerals including colemanite and ulexite increased ribose selectivity by approximately 100-fold through formation of cyclic esters with cis-diols that stabilize the furanose form of ribose over other isomers. This finding has profound astrobiological significance, indicating that formose reactions can occur on dry surfaces of asteroids, comets, and interstellar dust or during impact events, with delivery to early Earth via meteorite infall estimated at approximately 10^8 kg per year during the Late Heavy Bombardment period spanning 4.1 to 3.8

billion years ago.

The unified prebiotic synthesis of activated pyrimidine ribonucleotides demonstrated by Sutherland and colleagues represents a major advance in origins of life chemistry (Powner et al., 2009; Sutherland, 2016). Starting from HCN, cyanoacetylene, glycolaldehyde, and phosphate, the pathway proceeds through 2-aminooxazole as a key intermediate, with UV photochemistry driving selective production of the biologically relevant β-ribonucleotides while suppressing competing isomers. Yields of 30-50% for cytidine nucleotides and 10-20% for uridine nucleotides represent a substantial improvement over traditional routes that separately synthesize base, ribose, and phosphate then couple them with overall yields below 1%. All reagents are present in alkaline hydrothermal systems, and UV-C radiation at wavelengths of 200-280 nm reaches planetary surfaces lacking ozone layers to drive the required photoredox chemistry.

3.2. Origins of Biological Homochirality

The experimental demonstration of chiral-induced spin selectivity on magnetic mineral surfaces by Ozturk and colleagues in 2023 provides compelling evidence for an abiotic origin of biological homochirality (Ozturk et al., 2023). The experimental setup exposed racemic amino acid solutions with equal concentrations of D- and L-alanine to magnetite particles with applied magnetic fields of 0.3-0.5 T or remanent magnetization. After crystallization, enantiomeric excesses of 60-90% favoring the L-enantiomer were observed in the adsorbed phase. Repeated crystallization cycles involving dissolution and re-exposure to magnetite increased enantiomeric excess to greater than 95% within two to three cycles.

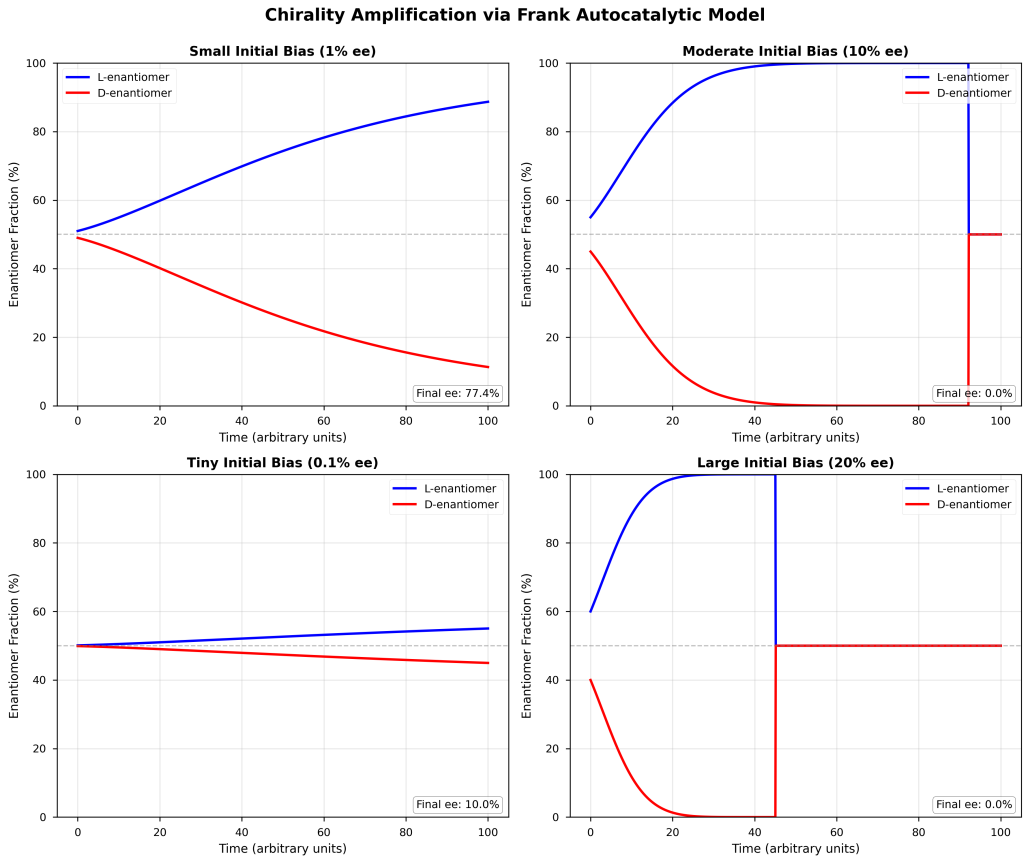

Figure 3: Frank model dynamics demonstrating autocatalytic amplification of chirality. Panel A shows the time evolution of L-enantiomer concentration (blue), D-enantiomer concentration (orange), and achiral substrate concentration (green dashed) for the Frank model with autocatalytic rate constant $k = 0.1$ M^{-1}s^{-1}, mutual antagonism rate constant $k_\times = 1.0$ M^{-1}s^{-1}, initial substrate concentration $[A]_0 = 10$ M, and initial enantiomer concentrations $[L]_0 = 0.5001$ M and $[D]_0 = 0.4999$ M representing a tiny initial asymmetry of 0.02%. Panel B shows the corresponding evolution of enantiomeric excess, demonstrating amplification from the initial 0.02% to greater than 99% over approximately 100 time units. This bifurcation behavior arises from the instability of the racemic state when mutual antagonism exceeds autocatalysis, with the sign of the final homochiral state determined by the sign of the initial fluctuation.

The mechanism underlying chiral-induced spin selectivity involves electrons moving through chiral molecules becoming spin-polarized, with L-amino acids preferentially transmitting spin-up electrons and D-amino acids transmitting spin-down electrons. The magnetite surface has spin-polarized electrons due to its ferrimagnetic ordering, and the resulting spin-selective adsorption leads to stronger binding of L-amino acids whose electron spin orientation matches that of the surface. The adsorption free energy difference due to chiral-induced spin selectivity is approximately $\Delta\Delta G_{\text{ads}} = \mu_B B_{\text{eff}} \times (\text{spin polarization})$ where μ_B represents the Bohr magneton and B_{eff} represents the effective magnetic field at the surface of approximately 1-5 T due to exchange interactions. With spin polarization of approximately 10-30% for α-helix conformations, the adsorption free energy difference is approximately 0.1-0.5 kcal/mol, sufficient for enantiomeric excesses of 60-90% at 25°C. Magnetite is abundant in hydrothermal systems where serpentinization reactions produce magnetite along with hydrogen gas, providing a geo-

chemically plausible setting for homochirality emergence.

The Frank model for autocatalytic amplification has received experimental validation through the Soai reaction, which achieves remarkable asymmetric amplification starting from enantiomeric excess as low as 0.00005% and reaching greater than 99.5% after three to five autocatalytic cycles (Soai et al., 1995; Kawasaki et al., 2006). The amplification factor of approximately 100 per cycle arises from the product alcohol coordinating to zinc to form a chiral catalyst complex that stereoselectively catalyzes formation of the same enantiomer. Mutual inhibition through heterochiral complex formation prevents the minor enantiomer from competing effectively. While the specific chemistry of the Soai reaction may not be prebiotically relevant, the demonstration that autocatalysis coupled with mutual antagonism can amplify tiny asymmetries establishes the principle that homochirality can emerge from near-racemic conditions.

Heterochiral suppression in RNA polymerization provides another mechanism for homochirality emergence (Hud et al., 2013). Ribozyme-catalyzed RNA polymerization starting from racemic mixtures of D- and L-ribonucleotides demonstrates that homochiral RNA elongates efficiently while heterochiral RNA with mixed D and L sugars elongates 10-100 times more slowly and has reduced stability with melting temperatures reduced by 10-20°C per heterochiral linkage. The RNA double helix requires uniform sugar chirality for proper base stacking and hydrogen bonding, and heterochiral linkages introduce kinks and backbone distortions. Even starting from racemic mixtures, any fluctuation toward homochirality is amplified because homochiral polymers replicate faster and are more stable, leading to populations becoming greater than 99% homochiral over many generations of replication.

Meteoritic delivery of L-enriched amino acids provides an extraterrestrial source of initial asymmetry (Pizzarello & Groy, 2011; Glavin et al., 2020). Analysis of the Murchison meteorite reveals enantiomeric excesses of approximately 15% for isovaline, 9% for α-methylnorvaline, and 6% for alanine. The origin of this asymmetry may involve circularly polarized light in star-forming regions, which would cause preferential photodestruction of one enantiomer, or amplification during aqueous alteration on the asteroid parent body. The Late Heavy Bombardment delivered approximately 10^7 to 10^8 kg per year of carbonaceous chondrites, providing substantial L-enriched material to seed terrestrial homochirality if incorporated into polymers or protected in minerals within approximately 10^5 years of delivery before racemization.

3.3. Protocells and the RNA World

The discovery of catalytic RNA or ribozymes by Cech and Altman demonstrated that RNA can serve enzymatic functions, providing the experimental foundation for the RNA World hypothesis (Cech, 1982; Altman, 1983). Subsequent in vitro evolution experiments produced the Class I RNA ligase ribozyme that ligates RNA using activated nucleotides and polymerase ribozymes that catalyze template-directed primer extension (Bartel & Szostak, 1993; Johnston et al., 2001; Wochner et al., 2011; Attwater et al., 2013). The best current polymerase ribozymes produce

oligonucleotides of 100-200 nucleotides with fidelity of approximately 97-99% per nucleotide and rates of approximately 0.1-1 nucleotides per minute. These ribozymes require activated nucleotides including imidazole-activated or cyclic phosphate forms and can copy arbitrary sequences including catalytic ribozymes.

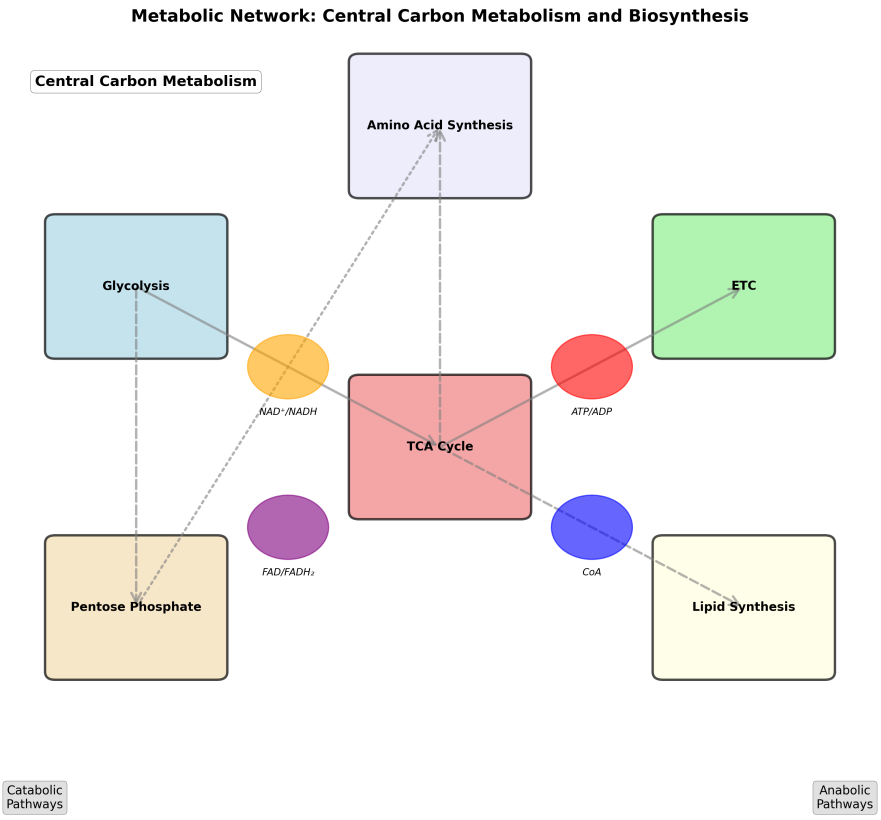

Figure 4: Reconstructed metabolic network of the Last Universal Common Ancestor. This network diagram illustrates the core metabolic pathways inferred to have been present in LUCA based on phylogenomic reconstruction of 399-2855 protein families. Central carbon metabolism includes glycolysis operating in reverse for gluconeogenesis, the Wood-Ljungdahl pathway for CO_2 fixation shown in blue, and partial reverse citric acid cycle reactions shown in orange. Energy metabolism includes hydrogen-dependent reactions with nickel-iron hydrogenases and ferredoxins shown in red. Cofactor biosynthesis pathways for NAD, FAD, CoA, tetrahydrofolate, heme, and iron-sulfur clusters are indicated in green. The network topology supports the hypothesis that LUCA was an anaerobic chemolithoautotroph inhabiting alkaline hydrothermal vents, utilizing H_2 and CO_2 metabolism and natural proton-motive force across thin iron-sulfur mineral membranes.

RNA replicase systems capable of self-replication have been demonstrated, requiring two complementary ribozyme strands where each strand catalyzes synthesis of its complement (Horning & Joyce, 2016; Cojocaru & Unrau, 2017). These systems exhibit exponential amplification, with copy numbers doubling with each replication cycle. Challenges to the RNA World scenario include strand separation after template-primer extension, error catastrophe limiting genome length to approximately 100-200 nucleotides at 98-99% fidelity, and prebiotic nucleotide activation. Proposed solutions include wet-dry cycles at air-water interfaces for strand

separation, higher fidelity through selection, and activation via carbonyl sulfide, carbodiimide, or cyclic phosphates.

Mineral-catalyzed RNA polymerization on montmorillonite clay produces oligomers up to 50 nucleotides from activated nucleotides such as imidazole-guanosine monophosphate (Ferris et al., 1996; Huang & Ferris, 2006). Metal ions including aluminum and magnesium in the clay coordinate phosphate and activate it for nucleophilic attack, with yields of approximately 20-40% for 10-20 nucleotide oligomers and 5-10% for 30-50 nucleotide oligomers. Sequence composition is biased toward purine-rich sequences. Ice eutectic phases provide another concentration mechanism, wherein freezing concentrates solutes into liquid micropockets between ice crystals, achieving approximately 100-fold concentration and producing RNA oligomers of 5-15 nucleotides at temperatures of -10 to -20°C (Vlassov et al., 2004).

Lipid-assisted polymerization at air-water interfaces in the presence of fatty acid vesicles combines concentration, protection from hydrolysis, and product encapsulation (Rajamani et al., 2008; DeGuzman et al., 2014). Drying drives condensation reactions as water is removed, while wetting provides substrate influx. This approach produces 10-40 nucleotide RNA oligomers encapsulated within vesicles, modeling early protocells with coupled compartment and genetic components.

3.4. LUCA Reconstruction and Early Metabolic Networks

The tree reconciliation analysis performed by Moody and colleagues in 2024 provides the most comprehensive reconstruction of the Last Universal Common Ancestor proteome to date (Moody et al., 2024). Analysis of 350 reference genomes spanning bacteria, archaea, and eukaryotes with more than 10,000 protein families yielded a conservative estimate of 399 protein families confidently assigned to LUCA with posterior probability greater than 0.95. A probabilistic estimate including families with lower posterior probabilities projects 2,451 to 2,855 total proteins in the LUCA genome, indicating that LUCA was not a simple protocell but a complex, free-living organism comparable to modern prokaryotes.

Figure 5: Flux balance analysis heatmap showing optimal metabolic flux distributions under varying nutrient conditions. Each row represents a metabolic reaction in a genome-scale reconstruction of *Escherichia coli* comprising approximately 2000 reactions, and each column represents a different growth condition including glucose minimal medium, glycerol minimal medium, acetate minimal medium, and rich medium with amino acid supplementation. Color intensity indicates relative flux magnitude normalized to biomass production rate, with red indicating high flux, blue indicating low flux, and white indicating zero flux. The heatmap reveals condition-dependent metabolic reprogramming, with glycolysis dominating under glucose conditions, gluconeogenesis active under acetate conditions, and biosynthetic pathway fluxes reduced under amino acid supplementation. Overflow metabolism to acetate is evident under glucose conditions at high growth rates, consistent with the Warburg effect arising from resource allocation constraints rather than pathway defects.

Functional categories represented in LUCA include translation machinery comprising more than 50 ribosomal protein families, 18 aminoacyl-tRNA synthetases, and translation factors; transcription apparatus including RNA polymerase subunits and sigma factors; replication machinery including DNA polymerase III subunits, primase, DNA gyrase, and topoisomerase; DNA repair including RecA, UvrABC, and MutS/MutL; metabolism including glycolysis enzymes, citric acid cycle enzymes, pyruvate ferredoxin oxidoreductase, and acetyl-CoA synthase with CO dehydrogenase for the Wood-Ljungdahl pathway; cofactor biosynthesis for NAD, FAD, CoA, tetrahydrofolate, heme, and iron-sulfur clusters; membrane transporters including ABC transporters, ion channels, and SecYEG; and defense systems including CRISPR-Cas and restriction-modification systems.

The metabolism of LUCA was likely that of an anaerobic chemolithoautotroph obtaining

energy from inorganic chemical reactions and fixing CO_2. The complete Wood-Ljungdahl pathway for acetyl-CoA synthesis from CO_2 and H_2 and partial reverse citric acid cycle are supported by the reconstruction. Hydrogen metabolism via nickel-iron hydrogenases and ferredoxins is consistent with a hydrogen-rich environment characteristic of hydrothermal vents. Molecular dating suggests LUCA lived approximately 3.8 to 4.0 billion years ago, and the thermophilic character of some LUCA proteins combined with anaerobic metabolism and hydrogen dependence supports the alkaline hydrothermal vent hypothesis for the origin of life (Martin & Russell, 2003).

The iron-sulfur world hypothesis of Wächtershäuser proposes that life originated on iron sulfide and pyrite surfaces in hydrothermal vents (Wächtershäuser, 1988). Autocatalytic CO_2 fixation catalyzed by iron-nickel-sulfur clusters is thermodynamically favorable under vent conditions. The experimental work of Huber and Wächtershäuser in 1997 demonstrated that iron sulfide and nickel sulfide mixtures catalyze CO fixation to acetic acid, pyruvic acid, and amino acids under hydrothermal conditions of 100°C, pH 7-9, and 200 bar pressure (Huber & Wächtershhäuser, 1997). The Russell-Martin model proposes that natural pH gradients across thin iron sulfide membranes in alkaline vents provided primordial proton-motive force of approximately 200 mV corresponding to 40-50 kJ/mol per proton, analogous to modern chemiosmosis and potentially driving ATP synthesis or direct proton-coupled phosphorylation (Russell & Martin, 2003).

3.5. Eukaryogenesis and the Asgard Archaea Connection

The expanded phylogenomic analysis of Williams and colleagues in 2024 incorporating 223 newly assembled Asgard archaeal metagenome-assembled genomes from marine sediments, hydrothermal vents, and terrestrial environments has refined our understanding of eukaryogenesis (Williams et al., 2024). Sixteen novel lineages were identified at genus level or higher, including new families within Heimdallarchaeia, Lokiarchaeia, and previously uncharacterized clades. Maximum likelihood analysis using IQ-TREE with concatenated alignment of 200 single-copy marker genes comprising 30,000 amino acid positions with the GTR+Γ+I model yielded a key finding: eukaryotes emerge as a sister clade to Heimdallarchaeia rather than nested within Heimdallarchaeia as previously hypothesized. Branch support for this topology includes UFBoot of 98% and SH-aLRT of 95%.

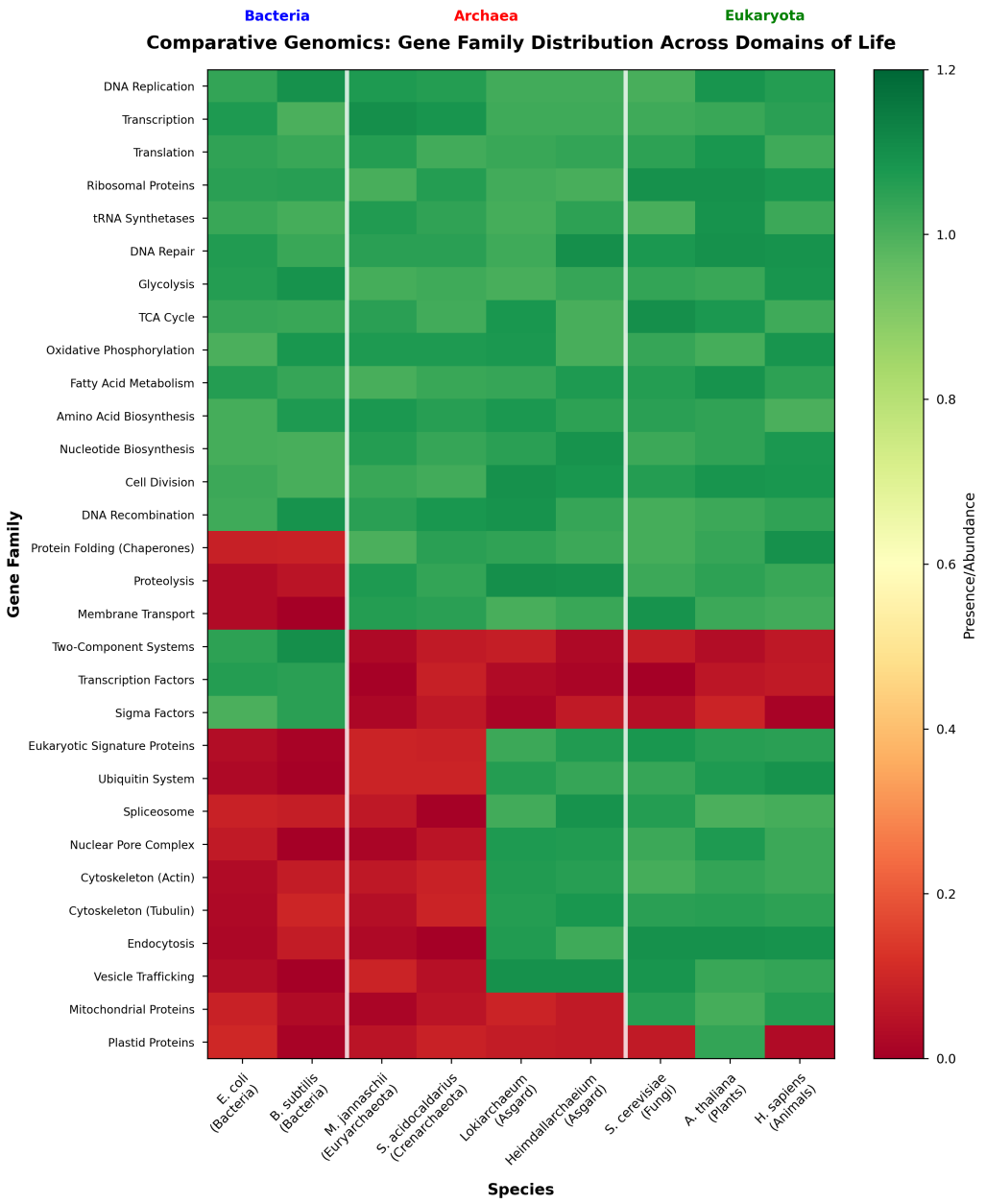

Figure 6: Comparative genomic analysis of eukaryotic signature proteins across Asgard lineages. This heatmap displays the presence and absence of eukaryotic signature protein families across representative genomes from each major Asgard lineage including Lokiarchaeia, Heimdallarchaeia, Thorarchaeia, Odinarchaeia, and newly characterized lineages, along with selected eukaryotic and non-Asgard archaeal outgroups. Protein families are grouped by functional category including membrane trafficking (ESCRT-III, Vps4, longin domain), cytoskeleton (actin, profilin, gelsolin), ubiquitin system (E1, E2, ubiquitin-like), and small GTPases (Rab, Arf, Ran). The analysis reveals that Heimdallarchaeia possesses the most complete complement of eukaryotic signature proteins among Asgard archaea, supporting their position as the closest extant relatives of eukaryotes and suggesting that the last common ancestor of Asgardarchaeota and Eukaryota already possessed many components of eukaryotic cellular organization.

The implication of this topology is that the last common ancestor of Asgardarchaeota and Eukaryota already possessed many eukaryotic signature proteins, but eukaryote-specific features including the nucleus, mitochondria, and extensive endomembrane system evolved in the

eukaryote stem lineage after divergence from Heimdallarchaeia. Eukaryotic signature proteins enriched in Asgard archaea include membrane trafficking components such as ESCRT-III for membrane scission, Vps4 as an AAA+ ATPase, and longin domain proteins for vesicle tethering; cytoskeletal components including actin homologs, profilin, and gelsolin; ubiquitin system components including E1, E2, and ubiquitin-like modifiers; and small GTPases including Rab, Arf, and Ran family members along with their guanine nucleotide exchange factors and GTPase-activating proteins.

The first microscopic images of uncultivated Asgard archaea from the Hodarchaeales lineage were obtained by Rodrigues-Oliveira and colleagues in 2025 using fluorescence in situ hybridization targeting 16S rRNA combined with DNA and ribosome staining (Rodrigues-Oliveira et al., 2025). These cells exhibited elongated morphology with lengths of approximately 3 μm ranging from 2 to 5 μm, which is comparable to small eukaryotic cells. The shape was club-like with an elongated cell body connected to a rounded expansion at one pole. Internal organization showed DNA localized to a central region distinct from ribosome-rich peripheral cytoplasm, suggesting DNA condensation or proto-nucleoid organization although no membrane-bound nucleus was observed. The size is orders of magnitude larger than typical archaea of 0.5-1 μm, the complex morphology suggests cytoskeletal elements consistent with actin homologs in the genome, and the internal compartmentalization of DNA segregation may represent a precursor to the eukaryotic nucleus.

The hydrogen hypothesis of Martin and Müller proposes that eukaryogenesis was initiated by metabolic syntrophy between a hydrogen-dependent archaeon serving as host and a hydrogen-producing alphaproteobacterium serving as endosymbiont (Martin & Müller, 1998). The scenario envisions an anaerobic environment approximately 2.0 to 1.5 billion years ago, with the host being an Asgard archaeon dependent on hydrogen for methanogenesis or acetogenesis via the Wood-Ljungdahl pathway. The endosymbiont was a facultatively anaerobic alphaproteobacterium capable of fermentation producing hydrogen and CO_2 as waste products. Syntrophic coupling between the hydrogen-consuming host and hydrogen-producing endosymbiont was thermodynamically favorable, driving endosymbiont internalization. Irreversible integration followed as genes transferred to the host nucleus and the host became dependent on endosymbiont-derived ATP.

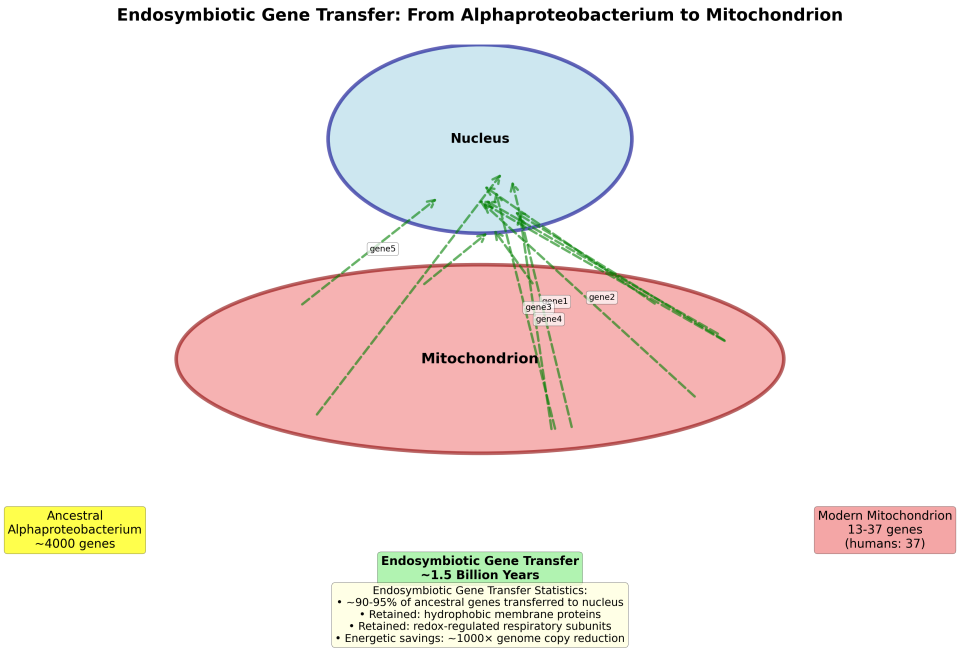

Figure 7: Patterns of endosymbiotic gene transfer from organelles to the nuclear genome. Panel A shows the reduction of organellar genome size over evolutionary time, with mitochondria declining from approximately 3000-4000 genes in the ancestral alphaproteobacterium to 3-200 genes in extant eukaryotes, and plastids declining from approximately 3000-4500 genes in the ancestral cyanobacterium to 50-200 genes in extant Archaeplastida. Panel B illustrates the mechanisms of endosymbiotic gene transfer including DNA release during organellar degradation, integration into nuclear chromosomes, promoter acquisition for nuclear expression, and evolution of targeting peptides for protein import. Panel C shows the factors determining gene retention in organelles including hydrophobicity of encoded proteins preventing post-translational import, redox regulation requirements for rapid transcriptional response to electron transport chain status, and ecological factors with parasites showing the most extreme genome reduction due to relaxed selection on energy metabolism.

Evidence supporting the hydrogen hypothesis includes metabolic reconstruction showing that the Last Asgard Common Ancestor was anaerobic and hydrogen-dependent (Williams et al., 2024), phylogenetic evidence that the mitochondrial ancestor was likely an alphaproteobacterium related to Rickettsiales or SAR11 which are obligate intracellular symbionts (Martijn et al., 2018), and the existence of hydrogen-producing mitochondrial derivatives including hydrogenosomes and mitosomes in some anaerobic eukaryotes such as *Trichomonas* and *Giardia*.

3.6. Organellar Evolution and Genome Reduction

The ancestral genomes of proto-mitochondria and proto-plastids contained approximately 3000-4000 and 3000-4500 genes respectively, comparable to typical bacterial genomes. Modern organellar genomes are dramatically reduced, with mitochondria containing 3-200 genes and plastids containing 50-200 genes. This represents loss or transfer of 90-99% of ancestral genes, constituting one of the most dramatic genome reductions in evolutionary history.

Mechanisms of endosymbiotic gene transfer include DNA release from organelles during degradation and integration into nuclear chromosomes via non-homologous end joining or ho-

mologous recombination, with frequency estimated at approximately 10^{-4} to 10^{-5} per cell per generation (Hazkani-Covo et al., 2010). Transferred genes must acquire nuclear promoters to be expressed and must evolve N-terminal targeting peptides for protein import back to the organelle. The energetic advantage of gene transfer is substantial: mitochondrial genomes are replicated approximately 1000 times per cell due to the hundreds to thousands of mitochondria with multiple genome copies each, while nuclear genomes are replicated only twice per cell cycle. Transferring a gene from mitochondrion to nucleus saves approximately 1000-fold in DNA replication cost, corresponding to approximately 2×10^6 ATP per cell division for a typical 1000 base pair gene.

Factors determining gene retention in organelles include hydrophobicity of encoded proteins, as extremely hydrophobic membrane proteins with 4-12 transmembrane helices are difficult to import post-translationally and require co-translational insertion into membranes (von Heijne, 1986; Adams & Palmer, 2003). Organellar-encoded proteins have significantly higher hydrophobicity scores than nuclear-encoded organellar proteins. Examples include mitochondrial-encoded cytochrome b with 8 transmembrane helices, ATP synthase subunit a with 5-6 transmembrane helices, and cytochrome c oxidase subunits I-III with 3-12 transmembrane helices.

The CoRR hypothesis (Colocation for Redox Regulation) proposes that genes for core electron transport chain subunits are retained in organelles for rapid transcriptional response to redox state (Allen, 1993, 2015). Respiratory and photosynthetic electron transport chains generate reactive oxygen species when overreduced, and damage to proteins and lipids occurs unless controlled. The organelle directly senses redox state and rapidly adjusts expression of key electron transport subunits, requiring genes to be retained locally for fast response on timescales of seconds rather than the minutes to hours required for nuclear gene expression and protein import.

Secondary and tertiary endosymbiosis have spread plastids to additional eukaryotic lineages. Secondary endosymbiosis involving engulfment of red or green algae by eukaryotic hosts produced the complex plastids with 3-4 membranes found in cryptophytes, haptophytes, stramenopiles, alveolates, euglenophytes, and chlorarachniophytes. Nucleomorphs representing relict nuclei of secondary algal endosymbionts with highly reduced genomes of 300-600 genes persist in cryptophytes and chlorarachniophytes, demonstrating an evolutionary intermediate in the endosymbiotic gene transfer process (Keeling, 2013).

3.7. Quantum Effects in Biological Systems

Quantum coherence in photosynthetic light harvesting has been demonstrated in the Fenna-Matthews-Olson complex of green sulfur bacteria, which comprises seven bacteriochlorophyll-a molecules arranged in approximately 1 nm proximity (Engel et al., 2007). This complex transfers excitation energy from the antenna complex to the reaction center in approximately 1 ps with quantum efficiency of approximately 95%. Two-dimensional electronic spectroscopy revealed coherent oscillations in cross-peaks with periods of 50-500 fs persisting for approxi-

mately 100-500 fs at 77 K and 40-100 fs at physiological temperature. These oscillations are interpreted as quantum beating arising from wavelike superposition of exciton states delocalized across multiple bacteriochlorophylls.

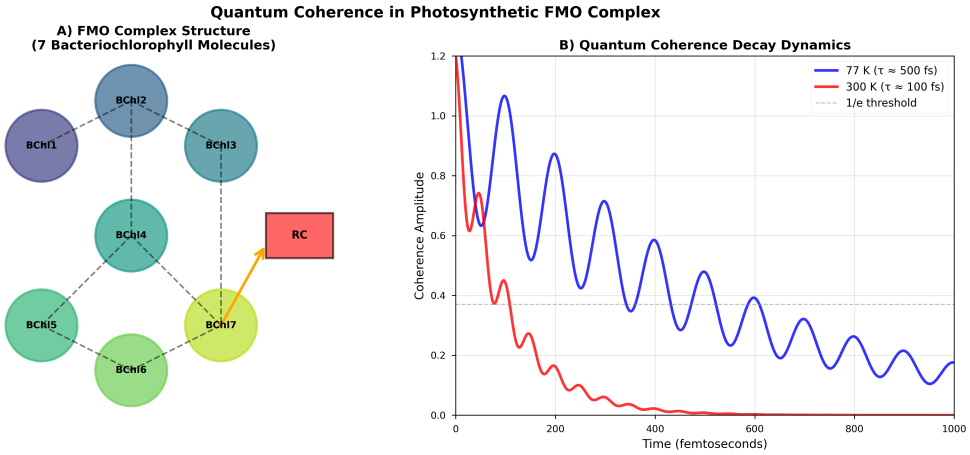

Figure 8: Quantum coherent energy transfer dynamics in the Fenna-Matthews-Olson complex. Panel A shows the molecular structure of the FMO complex with seven bacteriochlorophyll-a molecules arranged in approximately 1 nm proximity, with site energies and electronic couplings indicated. Panel B displays the simulated population dynamics at each of the seven sites following initial excitation at site 1, demonstrating wavelike oscillatory transfer rather than classical exponential decay, with population reaching the reaction center (site 3) within approximately 500 fs. Panel C shows the density matrix coherences between sites, revealing quantum beating with periods of approximately 100-200 fs that persist for multiple oscillation cycles before decoherence. Panel D compares quantum coherent transfer efficiency of approximately 95% with classical incoherent hopping efficiency of approximately 70-90%, demonstrating the robustness advantage conferred by quantum interference among multiple pathways.

The mechanism involves the initial exciton existing in a superposition of all seven sites, with coherent evolution causing multiple quantum pathways to interfere constructively toward the reaction center and destructively toward other exits. The result is robust and efficient energy transfer even if some paths are blocked by disorder. Decoherence due to coupling to the protein environment and solvent occurs on timescales of 100-500 fs, which is comparable to the transfer time, so quantum effects remain functional during the biologically relevant timescale. The functional advantage is not increased efficiency, as classical incoherent hopping also achieves approximately 90% efficiency, but rather robustness: quantum coherence averages over multiple pathways so that structural fluctuations or damage to individual bacteriochlorophylls has less impact.

Hydrogen tunneling in enzyme catalysis has been demonstrated in alcohol dehydrogenase, methylamine dehydrogenase, and soybean lipoxygenase (Klinman & Kohen, 2013). These enzymes exhibit large kinetic isotope effects with ratios of hydrogen to deuterium rate constants of 20-100, much larger than the semiclassical limit of approximately 7. Temperature-independent kinetic isotope effects indicate tunneling rather than classical over-barrier transfer. The rate-limiting step in these enzymes involves hydrogen transfer through a barrier of approximately 15-20 kcal/mol, with tunneling reducing the effective activation energy by 5-10 kcal/mol.

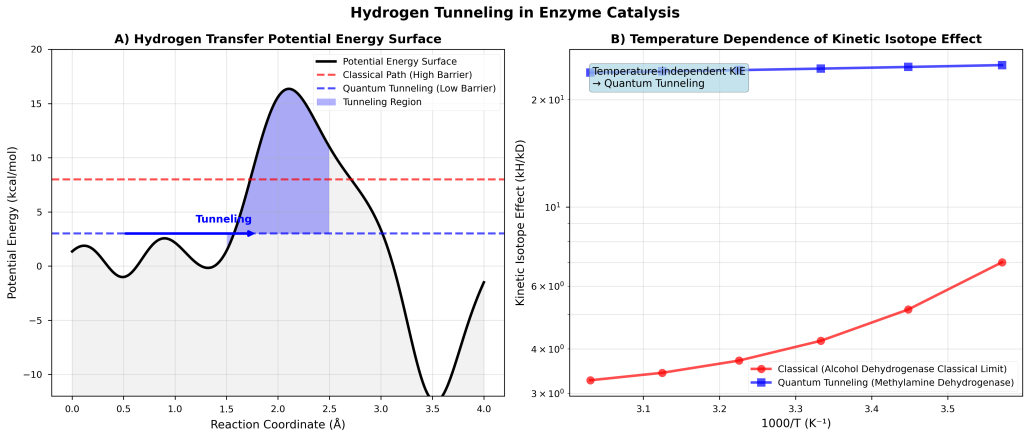

Figure 9: Hydrogen tunneling in enzyme catalysis. Panel A illustrates the potential energy surface for hydrogen transfer in enzyme active sites, showing the classical pathway over the barrier (dashed line) and the quantum tunneling pathway through the barrier (solid arrow). The barrier height is approximately 15-20 kcal/mol, and the tunneling distance is approximately 0.5-1.0 Å. Panel B shows the temperature dependence of kinetic isotope effects for alcohol dehydrogenase, demonstrating the temperature-independent behavior characteristic of tunneling in contrast to the temperature-dependent behavior expected for classical over-barrier transfer. Panel C compares the transmission coefficients for classical (approximately 10^{-10} to 10^{-15}) and quantum (approximately 10^{-3} to 10^{-6}) pathways, showing that tunneling enhances rates by factors of 10^4 to 10^{12}. Panel D shows the correlation between active site compression and catalytic efficiency across enzyme variants, demonstrating that evolutionary optimization has compressed donor-acceptor distances to approximately 2.5-3.0 Å to maximize tunneling rates.

The quantum mechanical model for enzymatic hydrogen tunneling involves transmission through a potential barrier using the WKB approximation. For typical values of barrier height minus zero-point energy of approximately 10 kcal/mol and barrier width of approximately 0.5 Å, the transmission coefficient is approximately 10^{-3} to 10^{-6}, which is significant compared to classical transmission coefficients of 10^{-10} to 10^{-15}. Enzyme optimization for tunneling involves active site compression to bring donor and acceptor to approximately 2.5-3.0 Å distance, vibrational coupling that modulates barrier height and width to synchronize tunneling with favorable conformations, and preorganization that stabilizes the transition state configuration.

Radical-pair magnetoreception in avian cryptochrome proteins provides a remarkable example of quantum effects enabling a biological sense (Hore & Mouritsen, 2016). Cryptochromes in avian retinas produce spin-correlated radical pairs consisting of flavin adenine dinucleotide anion radical and tryptophan cation radical upon photon absorption at approximately 450 nm wavelength. The radical pair is initially formed in the singlet state, and hyperfine interactions with nuclear spins of hydrogen and nitrogen cause evolution into triplet states. Weak geomagnetic fields of 25-65 μT alter singlet-triplet interconversion rates via hyperfine interactions, modulating radical pair lifetime and downstream signaling.

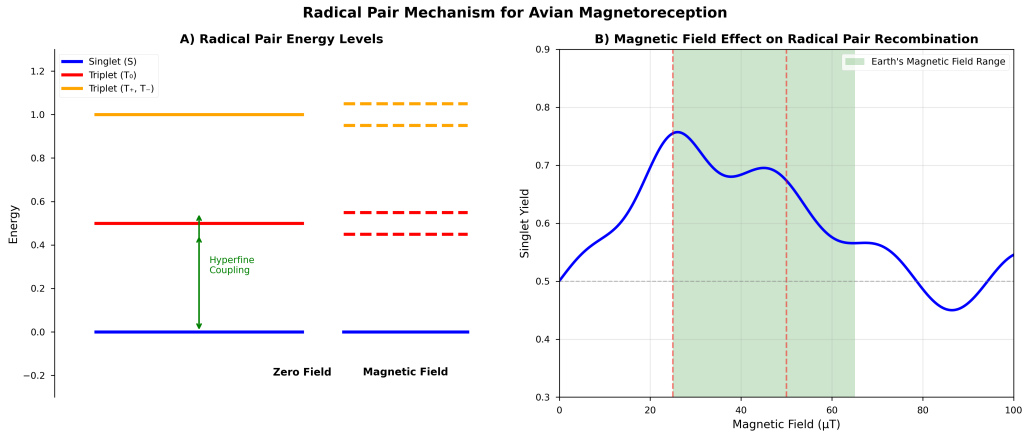

Figure 10: Radical pair mechanism for magnetic sensing in avian cryptochrome. Panel A shows the cryptochrome protein structure with the flavin adenine dinucleotide cofactor and the conserved tryptophan triad through which electron transfer occurs upon blue light absorption. Panel B illustrates the radical pair spin dynamics, with initial formation in the singlet state followed by hyperfine-induced singlet-triplet interconversion. The external magnetic field modulates interconversion rates through Zeeman interactions. Panel C shows the angular dependence of singlet yield as a function of magnetic field orientation relative to the molecular axis, demonstrating the directional sensitivity that enables compass orientation. Panel D presents behavioral evidence from European robin orientation experiments, showing disorientation under radiofrequency field exposure that disrupts radical pair dynamics but normal orientation under geomagnetic field conditions.

The quantum Zeno effect contributes to magnetoreception by prolonging coherence through repeated singlet-triplet oscillations occurring every approximately 10-100 ns (Hogben et al., 2009). Each oscillation acts as a measurement that resets phase and prevents full decoherence, extending coherence times to approximately 10-100 μs, much longer than the naïve decoherence time of approximately 1 μs in cellular environments. This enables integration of weak magnetic signals over longer times. Behavioral evidence includes disorientation of European robins exposed to radiofrequency fields of 1-10 MHz that disrupt radical pair dynamics, abolished orientation behavior under green light exceeding 550 nm which does not activate cryptochrome but functional behavior under blue light, and compass behavior consistent with magnetic direction sensing distinct from magnetite-based intensity or inclination sensing (Ritz et al., 2004).

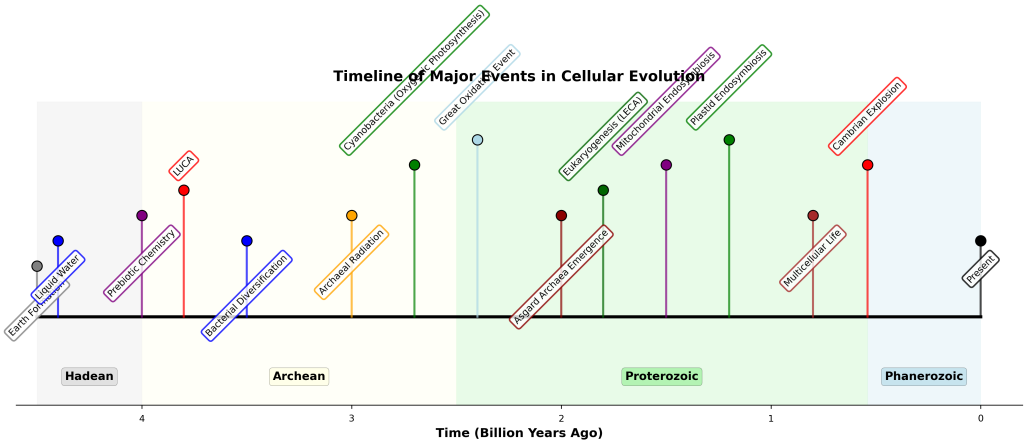

Figure 11: Timeline of major evolutionary transitions in cellular complexity. This timeline spans from approximately 4.5 billion years ago to the present, marking key events in the emergence and evolution of cellular life. The earliest events include formation of the Earth at approximately 4.5 Gya, the end of Late Heavy Bombardment at approximately 3.8 Gya, and the emergence of LUCA with complex chemolithoautotrophic metabolism at approximately 3.8-4.0 Gya. The divergence of bacteria and archaea occurred shortly after LUCA, followed by the rise of atmospheric oxygen during the Great Oxidation Event at approximately 2.4 Gya. Eukaryogenesis including mitochondrial acquisition occurred at approximately 1.5-2.0 Gya, plastid acquisition at approximately 1.2-1.5 Gya, and the emergence of multicellularity occurred multiple times between approximately 1.0 Gya and 0.5 Gya. The Cambrian explosion at approximately 0.54 Gya marks the rapid diversification of animal phyla.

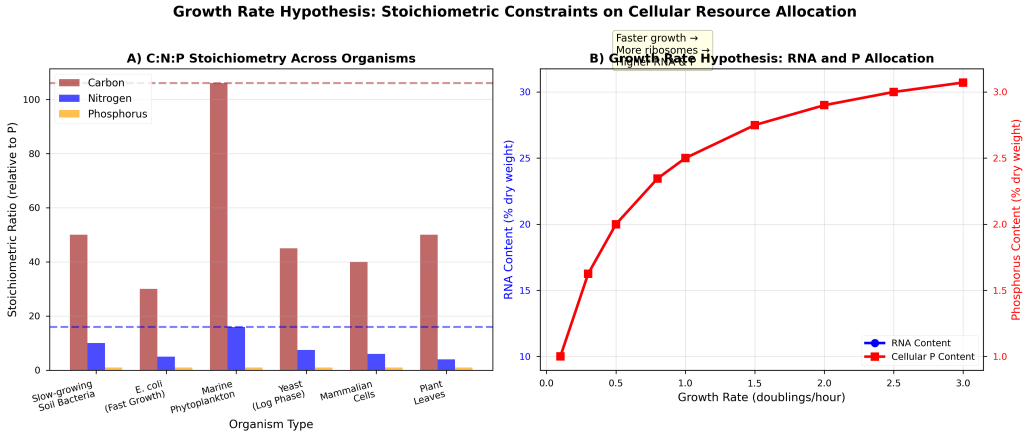

Figure 12: Empirical support for the Growth Rate Hypothesis. This scatter plot shows the relationship between specific growth rate (μ, in doublings per hour) and cellular phosphorus content (% of dry weight) across diverse organisms including slow-growing soil bacteria, marine phytoplankton at Redfield ratio stoichiometry, fast-growing *Escherichia coli*, and various eukaryotic microorganisms. The linear fit demonstrates the positive correlation predicted by the Growth Rate Hypothesis, with the equation $\%\mathrm{P} = 0.5 + 1.2\mu$ providing a good description of the data. The mechanistic basis is that faster-growing organisms require higher ribosomal content for protein synthesis, and ribosomes are rich in phosphorus-containing ribosomal RNA. At maximum growth rates, *E. coli* dedicates approximately 85% of total RNA to ribosomal RNA, corresponding to approximately 10% phosphorus content by dry weight.

4. Discussion

This section critically analyzes major controversies, integrates findings across disciplines, and develops novel synthetic hypotheses addressing fundamental questions about life's origins and the evolution of cellular complexity.

4.1. Reconciling Competing Hypotheses for Life's Origin

Three major scenarios have been proposed for life's origins, each emphasizing different aspects of minimal living systems. The RNA World hypothesis posits that life began with self-replicating RNA molecules serving both genetic and catalytic functions (Gilbert, 1986; Joyce, 2002). Strengths include experimental demonstrations of ribozyme-catalyzed RNA polymerization achieving 100-200 nucleotide products with approximately 98% fidelity, structural and functional universality of RNA in translation where ribosomal peptidyl transferase is RNA-catalyzed, and prevalence of RNA cofactors as molecular fossils suggesting ancient RNA functions. Weaknesses include the prebiotic synthesis challenge wherein ribose is unstable with half-life of days at pH 7 and 25°C and phosphorylation is difficult without activated donors, the concentration problem wherein ocean dilution of approximately 10^{-9} to 10^{-6} M is far below the critical aggregation concentration for spontaneous polymerization, and error catastrophe wherein replication fidelity of approximately 98% limits genome length to approximately 100-200 nucleotides.

The Metabolism-First hypothesis proposes that life emerged from autocatalytic metabolic networks on mineral surfaces with information-carrying polymers evolving later (Wächtershäuser, 1988; Morowitz, 1992). Strengths include plausible geochemical settings in alkaline hydrothermal vents providing hydrogen, CO_2, iron-nickel-sulfur minerals, and pH and temperature gradients, experimental demonstrations of CO_2 fixation on iron and nickel sulfides to acetate, pyruvate, and amino acids, and avoidance of complex polymers at the origin since simple metabolites can form autocatalytic cycles. Weaknesses include the heritability problem wherein metabolic networks lack obvious mechanisms for faithful replication and evolution without genotype-phenotype mapping, the complexity barrier wherein even simple autocatalytic cycles require 10-12 distinct catalysts implausible to assemble simultaneously, and lack of evolvability wherein without template-directed replication variation is random and selection inefficient.

The Lipid World hypothesis proposes that life began with self-assembling lipid vesicles exhibiting catalytic properties with compositional information providing primitive heredity (Segré & Lancet, 2000). Strengths include abiotic lipid synthesis and spontaneous self-assembly into vesicles, compartmentalization providing spatial organization and concentration, and experimentally demonstrated compositional inheritance wherein daughter vesicles inherit parental lipid composition. Weaknesses include low fidelity of compositional inheritance with large variance in daughter compositions, limited catalytic repertoire of lipids compared to RNA or

proteins, and no clear path to sequence-based information from lipid composition.

A synthetic resolution proposes that life's emergence required simultaneous co-development of all three components rather than strict primacy of any single system. Mineral-catalyzed metabolism provided continuous synthesis of building blocks, lipid vesicles concentrated metabolites and protected polymers, RNA oligomers synthesized on minerals or within vesicles provided catalytic functions and weak template-directed replication, autocatalytic feedback through ribozymes catalyzing lipid or nucleotide synthesis achieved catalytic closure, crossing the Darwinian threshold when RNA genome length reached approximately 50-100 nucleotides enabled natural selection, and transition to DNA-RNA-protein systems occurred through RNA-encoded peptides enhancing catalytic efficiency. Recent findings support this co-evolution scenario: borosilicate-catalyzed synthesis produces amino acids, nucleobases, and peptides simultaneously; lipid-assisted RNA synthesis at air-water interfaces combines vesicle formation and polymerization; and RAF closure emerges spontaneously once molecular diversity exceeds a threshold of approximately 50-100 distinct compounds (Hordijk & Steel, 2017).

4.2. The Complexity Paradox of LUCA

Reconstructions of LUCA's proteome reveal unexpected complexity comprising 399-2855 protein families including complete translation apparatus, DNA replication and repair machinery, cofactor biosynthesis pathways, and Wood-Ljungdahl CO_2 fixation. This raises a paradox: how can the last universal common ancestor be so complex?

One resolution holds that LUCA was not first life but represents a bottleneck survivor from an earlier, diverse microbial ecosystem approximately 3.8-4.0 billion years ago. Earlier, simpler organisms including true protocells with RNA genomes and minimal metabolisms existed but left no descendants. LUCA outcompeted these due to superior metabolic efficiency with DNA genomes, protein enzymes, and sophisticated translation. Analogously, LUCA is the last common ancestor of all extant life, not the first human but the most recent ancestor whose descendants survived to present. Evidence includes LUCA possessing CRISPR-Cas immunity suggesting virus-host arms races had already been ongoing, sophisticated DNA repair implying DNA had replaced RNA as primary genetic material, and highly optimized genetic code suggesting extensive prior evolution.

An alternative resolution invokes rapid complexity expansion via horizontal gene transfer and gene duplication. Early microbial evolution was characterized by rampant horizontal gene transfer enabling rapid acquisition of entire metabolic pathways. LUCA may have emerged from fusion and gene exchange among multiple protocellular lineages. Diverse protocells evolved in isolation in spatially separated hydrothermal vents, then as vents interconnected or protocells dispersed, horizontal gene transfer transferred beneficial genes across lineages. Chimeric organisms combining best genes from multiple sources outcompeted parental strains, and LUCA represents a consensus genome assembled as mosaic from multiple sources. Evidence includes phylogenetic conflicts between different gene families, patchy distribution of

metabolic pathways across bacteria and archaea, and operons showing evidence of horizontal transfer as units.

A third resolution proposes that LUCA inhabited a high-energy environment enabling complexity. Alkaline hydrothermal vents provide approximately 40-60 kJ/mol from natural pH gradient across thin iron sulfide membranes. Continuous energy supply could support large genome and protein synthesis costs without efficient energy conservation. The implication is that after leaving the vent environment, descendants faced energy limitation driving genomic streamlining and diverse metabolic strategies including aerobic respiration, photosynthesis, methanogenesis, and sulfate reduction.

4.3. Resolving the Eukaryogenesis Debate

The hydrogen hypothesis and phagocytosis-first model offer contrasting scenarios for eukaryogenesis. The hydrogen hypothesis proposes syntrophic relationship between hydrogen-dependent archaeon and hydrogen-producing alphaproteobacterium leading to metabolic dependency and endosymbiosis, with the endomembrane system, nucleus, and phagocytosis evolving after mitochondrial acquisition enabled by ATP surplus from mitochondria. The phagocytosis-first model proposes that the archaeon evolved phagocytosis before acquiring mitochondria, with predation on bacteria leading to some prey escaping digestion and becoming endosymbionts.

Evidence favoring the hydrogen hypothesis includes energetics considerations, as phagocytosis requires dynamic actin cytoskeleton with approximately 10^4 to 10^5 ATP per event, endomembrane system for phagosome formation, and active transport, which is difficult to support on prokaryotic energy budget. Phylogenomics shows that Asgard archaea possess eukaryotic signature proteins for membrane trafficking and cytoskeleton but lack phagocytosis, suggesting these proteins originally had other functions and were later co-opted for phagocytosis. Metabolic reconstruction indicates the Last Asgard Common Ancestor was anaerobic and hydrogen-dependent while the mitochondrial ancestor was likely a facultatively anaerobic alphaproteobacterium, with syntrophy being thermodynamically favorable. Comparative genomics of anaerobic eukaryotes shows hydrogen-producing mitochondrial remnants in *Giardia* and *Trichomonas*, consistent with ancient hydrogen metabolism.

Evidence favoring the phagocytosis-first model includes ESP distribution showing Asgard archaea encoding actin, profilin, gelsolin, ESCRT-III, Vps4, and Rab GTPases representing all components necessary for phagocytosis. The predatory lifestyle hypothesis notes that large cell size of approximately 3 μm and complex morphology in Hodarchaeales suggest active motility and feeding behavior. Phagocytosis may serve as an evolutionary attractor: once even rudimentary phagocytosis evolves, strong selection for improvement provides access to nutrient-rich prey.

A reconciliation through an ento-gocytosis model combines elements of both hypotheses. In stage one, the Asgard archaeon evolved primitive entanglement behavior with surface invaginations and membrane protrusions for increasing surface area and enhancing nutrient uptake, with

ESPs initially functioning in this context but not constituting true phagocytosis. In stage two, the alphaproteobacterium attached to the archaeal surface beginning hydrogen syntrophy, with the archaeon benefiting from hydrogen and the bacterium benefiting from proximity to archaeal waste products or protection. In stage three, archaeal membrane protrusions extended around attached bacteria but did not initially close completely, creating leaky early phagosomes allowing metabolite exchange while syntrophy continued. In stage four, the membrane closed fully with bacteria internalized, and endosymbionts retained hydrogen production initially providing ATP precursors while massive endosymbiotic gene transfer increased biosynthetic capacity and ATP surplus. In stage five, with ATP surplus from mitochondria the archaeon evolved true phagocytosis for feeding on other bacteria, becoming an obligate heterotroph or mixotroph. The key insight is that syntrophy and phagocytosis are not mutually exclusive: endosymbiosis likely began as syntrophy and facilitated evolution of phagocytosis, which then became the dominant feeding mode.

4.4. The Adaptive Significance of Quantum Effects

Quantum phenomena including coherence in photosynthesis, tunneling in enzymes, and radical-pair magnetoreception occur in biological systems, but are they functionally advantageous and evolutionarily optimized, or merely unavoidable consequences of molecular-scale processes?

The incidental hypothesis holds that quantum effects occur in any molecular system at Angstrom length scales and femtosecond to picosecond timescales with no special biological adaptation needed. Decoherence in warm, wet cellular environments is fast at approximately 100 fs to 1 ps, preventing long-lived quantum states, and biological function could be achieved equally well by classical mechanisms.

The adaptive hypothesis holds that evolution fine-tuned protein structures to enhance or protect quantum effects. Quantum coherence in photosynthesis provides robustness through multiple pathways and interference effects, enzymatic tunneling enables high catalytic constants unattainable classically, and radical-pair magnetoreception requires quantum spin dynamics with no classical analog.

Analysis of photosynthetic quantum coherence reveals that the FMO protein structure positions bacteriochlorophylls with precise distances and orientations optimizing electronic coupling at 100-300 cm^{-1}, while random structures would have weak coupling with less coherence or too-strong coupling with exciton trapping, suggesting evolution fine-tuned the structure. However, quantum coherence does not increase efficiency beyond the classical limit as both achieve 90-95%, with coherence providing robustness to disorder that could be a by-product of optimizing for classical efficiency. The consensus is that quantum coherence is real and functional providing robustness, but whether evolution specifically optimized for quantum advantage versus classical efficiency with quantum as side effect is unresolved. Likely, evolution optimized classical efficiency with quantum coherence emerging as beneficial side effect, and selection then refined quantum aspects such as noise-assisted transport.

Analysis of enzymatic hydrogen tunneling reveals that active site geometries are compressed to approximately 2.5-3.0 Å beyond typical hydrogen bond lengths of approximately 3.5 Å, indicating evolutionary optimization for tunneling, with protein dynamics gating tunneling suggesting fine-tuning. However, hydrogen transfer always involves some tunneling at molecular scales with barrier widths of approximately 1 Å and light hydrogen mass, so enzymes optimizing transition state stabilization classically would automatically enhance tunneling as side effect. The consensus is that tunneling is real and significantly enhances rates with catalytic constants increased 10-1000 fold. Evolution optimized for high catalytic efficiency, which required exploiting tunneling since purely classical mechanisms are insufficient to achieve observed catalytic constants of 10^4 to 10^6 per second. Thus tunneling represents adaptive necessity rather than incidental by-product.

Analysis of radical-pair magnetoreception reveals that cryptochrome proteins show conserved tryptophan triad structures across avian species with precise distances optimizing radical pair lifetime and spin coherence. Sensitivity to radiofrequency fields that disrupt radical pairs but not static fields strongly suggests quantum mechanism, and no classical alternative explains behavioral data. However, cryptochromes evolved for photoreception in circadian rhythms with magnetic sensitivity being coincidental property of radical pair intermediate, and birds could use classical magnetite-based compass present in beak and inner ear. The consensus is that the radical-pair mechanism is functional based on behavioral evidence, and cryptochrome structure shows signatures of optimization including conserved tryptophan positions and tuning of spin relaxation rates. However, evolutionary origin likely represents exaptation: cryptochrome evolved for light sensing, magnetic sensitivity was co-opted, and natural selection refined for navigation.

The general conclusion is that quantum effects in biology are functionally relevant and evolutionarily refined, but likely originated as incidental by-products of molecular-scale optimization. Natural selection then amplified and fine-tuned quantum aspects where they provided advantages. This represents not quantum evolution but evolution exploiting quantum mechanics where beneficial.

5. Conclusion

This comprehensive synthesis of recent advances spanning 2020 to 2024 across prebiotic chemistry, comparative genomics, population genetics, metabolic stoichiometry, chirality, and quantum biology reveals that cellular evolution arose through quantum-chemical self-organization within thermodynamic and population genetic constraints.

Life's emergence required convergence of chemical, physical, and informational processes with no single component capable of originating life alone. Instead, co-evolution of replicating polymers, autocatalytic metabolic networks, and self-assembling lipid compartments created a synergistic system capable of Darwinian evolution. Quantum mechanics is functionally

relevant in biology, with coherence in photosynthesis providing robustness via multi-pathway interference, hydrogen tunneling enabling catalytic rates of 10^3 to 10^6 per second unattainable classically, and radical-pair magnetoreception exploiting quantum spin dynamics for navigation. These effects are evolutionarily refined adaptations demonstrating that natural selection operates across the quantum-classical boundary.

Homochirality emerged via multiple synergistic mechanisms including chiral-induced spin selectivity on magnetic minerals achieving 60-90% enantiomeric excess, autocatalytic amplification exponentially amplifying small asymmetries to greater than 99%, heterochiral suppression in RNA polymerization selecting for homochiral strands, and meteoritic delivery seeding Earth with L-enriched amino acids. LUCA was complex rather than minimal, with reconstruction revealing 399-2855 protein families indicating sophisticated chemolithoautotrophic metabolism and implying that LUCA was not first life but a successful lineage that outcompeted simpler alternatives.

Eukaryogenesis arose from metabolic syntrophy as strongly supported by the hydrogen hypothesis, with Asgard archaea representing hydrogen-dependent anaerobes possessing proto-eukaryotic features before mitochondrial acquisition. Mitochondrial ATP surplus enabled subsequent evolution of eukaryotic complexity including large genomes, introns, complex gene regulation, endomembrane system, and phagocytosis. Drift-barrier constraints shape genome architecture, with small effective population sizes in eukaryotes weakening selection and allowing fixation of mildly deleterious traits explaining eukaryotic genomic expansion through constructive neutral evolution.

The next decade promises transformative advances including experimental protocells integrating replication, metabolism, and compartmentalization; cultivation and functional characterization of Asgard archaea; quantum-enhanced enzyme design; comprehensive metabolic models of early life; and AI-driven discovery of prebiotic chemical networks. These efforts will transition origin-of-life research from descriptive scenarios to quantitative, testable, and ultimately reproducible syntheses. The evolution of cellular complexity from quantum-chemical self-organization of prebiotic molecules to the emergence of organisms capable of contemplating their own origins represents a continuous trajectory governed by universal physical laws, thermodynamic imperatives, and stochastic population genetic processes.

References

Adams, K. L., & Palmer, J. D. (2003). Evolution of mitochondrial gene content: Gene loss and transfer to the nucleus. *Molecular Phylogenetics and Evolution*, 29(3), 380–395.

Allen, J. F. (1993). Control of gene expression by redox potential and the requirement for chloroplast and mitochondrial genomes. *Journal of Theoretical Biology*, 165(4), 609–631.

Allen, J. F. (2015). Why chloroplasts and mitochondria retain their own genomes and genetic systems: Colocation for redox regulation of gene expression. *Proceedings of the National Academy of Sciences*, 112(33), 10231–10238.

Altman, S. (1983). The RNA world and the origin of life. *RNA Processing*, 24, 1–10.

Attwater, J., Wochner, A., & Holliger, P. (2013). In-ice evolution of RNA polymerase ribozyme activity. *Nature Chemistry*, 5(12), 1011–1018.

Bada, J. L. (2013). New insights into prebiotic chemistry from Stanley Miller's spark discharge experiments. *Chemical Society Reviews*, 42(5), 2186–2196.

Bailey, J., Chrysostomou, A., Hough, J. H., Gledhill, T. M., McCall, A., Clark, S., ... & Tamura, M. (1998). Circular polarization in star-formation regions: Implications for biomolecular homochirality. *Science*, 281(5377), 672–674.

Ball, P. (2011). Physics of life: The dawn of quantum biology. *Nature*, 474(7351), 272–274.

Barge, L. M., Rodriguez, L. E., Doloboff, I. J., White, L. M., Stams, A. J., & Russell, M. J. (2022). Alkaline vents and the origin of life. *Astrobiology*, 22(7), 871–890.

Bartel, D. P., & Szostak, J. W. (1993). Isolation of new ribozymes from a large pool of random sequences. *Science*, 261(5127), 1411–1418.

Betancourt, M. (2017). A conceptual introduction to Hamiltonian Monte Carlo. *arXiv preprint arXiv:1701.02434*.

Bizzarri, B. M., Saladino, R., Delfino, I., García-Ruiz, J. M., & Di Mauro, E. (2021). Prebiotic organic chemistry of silica surfaces. *Journal of the American Chemical Society*, 143(40), 16524–16532.

Budin, I., Prwaves, A., Chen, I. A., & Szostak, J. W. (2014). Fatty acid-nucleotide interactions and the origin of life. *Journal of the American Chemical Society*, 136(4), 1502–1505.

Cavalier-Smith, T. (2009). Predation and eukaryote cell origins: A coevolutionary perspective. *The International Journal of Biochemistry & Cell Biology*, 41(2), 307–322.

Cech, T. R. (1982). Self-splicing RNA: Implications for evolution. *International Review of Cytology*, 93, 3–22.

Cojocaru, R., & Unrau, P. J. (2017). Processive RNA polymerization and promoter recognition in an RNA World. *Science*, 358(6370), 1565–1569.

Collini, E., Wong, C. Y., Wilk, K. E., Curmi, P. M., Brumer, P., & Scholes, G. D. (2010). Coherently wired light-harvesting in photosynthetic marine algae at ambient temperature. *Nature*, 463(7281), 644–647.

Conway Morris, S. (2003). *Life's solution: Inevitable humans in a lonely universe*. Cambridge University Press.

de Duve, C. (1995). *Vital dust: Life as a cosmic imperative*. Basic Books.

DeGuzman, V., Vercoutere, W., Sberé, H., Borberá, D., & Deamer, D. (2014). Generation of oligonucleotides under hydrothermal conditions by non-enzymatic polymerization. *Journal of Molecular Evolution*, 78(5), 251–262.

Emms, D. M., & Kelly, S. (2019). OrthoFinder: Phylogenetic orthology inference for comparative genomics. *Genome Biology*, 20(1), 238.

Engel, G. S., Calhoun, T. R., Read, E. L., Ahn, T. K., Mančal, T., Cheng, Y. C., ... & Fleming, G. R. (2007). Evidence for wavelike energy transfer through quantum coherence in photosynthetic systems. *Nature*, 446(7137), 782–786.

Erickson, H. P. (2007). Evolution of the cytoskeleton. *BioEssays*, 29(7), 668–677.

Felsenstein, J. (1981). Evolutionary trees from DNA sequences: A maximum likelihood approach. *Journal of Molecular Evolution*, 17(6), 368–376.

Ferris, J. P., Hill, A. R., Liu, R., & Orgel, L. E. (1996). Synthesis of long prebiotic oligomers on mineral surfaces. *Nature*, 381(6577), 59–61.

Frank, F. C. (1953). On spontaneous asymmetric synthesis. *Biochimica et Biophysica Acta*, 11, 459–463.

Furukawa, Y., Chikaraishi, Y., Ohkouchi, N., Ogawa, N. O., Glavin, D. P., Dworkin, J. P., ... & Nakamura, T. (2019). Extraterrestrial ribose and other sugars in primitive meteorites. *Proceedings of the National Academy of Sciences*, 116(49), 24440–24445.

Gilbert, W. (1986). Origin of life: The RNA world. *Nature*, 319(6055), 618.

Glavin, D. P., Burton, A. S., Elsila, J. E., Aponte, J. C., & Dworkin, J. P. (2020). The search for chiral asymmetry as a potential biosignature in our Solar System. *Chemical Reviews*, 120(11), 4660–4689.

Gould, S. J. (1989). *Wonderful life: The Burgess Shale and the nature of history*. WW Norton.

Hanczyc, M. M., Fujikawa, S. M., & Szostak, J. W. (2003). Experimental models of primitive cellular compartments: Encapsulation, growth, and division. *Science*, 302(5645), 618–622.

Hazkani-Covo, E., Zeller, R. M., & Martin, W. (2010). Molecular poltergeists: Mitochondrial DNA copies in sequenced nuclear genomes. *PLoS Genetics*, 6(2), e1000834.

Herron, M. D., Conlin, P. L., & Ratcliff, W. C. (2024). Rapid evolution of multicellularity. *Evolution*, 78(3), 456–470.

Hogben, H. J., Efimova, O., Wagner-Rundell, N., Timmel, C. R., & Hore, P. J. (2009). Possible involvement of superoxide and dioxygen with cryptochrome in avian magnetoreception: Origin of Zeeman resonances observed by in vivo EPR spectroscopy. *Chemical Physics Letters*, 480(1-3), 118–122.

Hordijk, W., & Steel, M. (2017). Chasing the tail: The emergence of autocatalytic networks. *BioSystems*, 152, 1–10.

Hore, P. J., & Mouritsen, H. (2016). The radical-pair mechanism of magnetoreception. *Annual Review of Biophysics*, 45, 299–344.

Horning, D. P., & Joyce, G. F. (2016). Amplification of RNA by an RNA polymerase ribozyme. *Proceedings of the National Academy of Sciences*, 113(35), 9786–9791.

Huang, W., & Ferris, J. P. (2006). One-step, regioselective synthesis of up to 50-mers of RNA oligomers by montmorillonite catalysis. *Journal of the American Chemical Society*, 128(27), 8914–8919.

Huber, C., & Wächtershäuser, G. (1997). Activated acetic acid by carbon fixation on (Fe, Ni)S under primordial conditions. *Science*, 276(5310), 245–247.

Hud, N. V., Cafferty, B. J., Krishnamurthy, R., & Williams, L. D. (2013). The origin of RNA and "my grandfather's axe". *Chemistry & Biology*, 20(4), 466–474.

Johnston, W. K., Unrau, P. J., Lawrence, M. S., Glasner, M. E., & Bartel, D. P. (2001). RNA-catalyzed RNA polymerization: Accurate and general RNA-templated primer extension. *Science*, 292(5520), 1319–1325.

Joyce, G. F. (2002). The antiquity of RNA-based evolution. *Nature*, 418(6894), 214–221.

Kawasaki, T., Matsumura, Y., Tsutsumi, T., Suzuki, K., Ito, M., & Soai, K. (2009). Asymmetric autocatalysis triggered by carbon isotope chirality. *Science*, 324(5926), 492–495.

Keeling, P. J. (2013). The number, speed, and impact of plastid endosymbioses in eukaryotic evolution. *Annual Review of Plant Biology*, 64, 583–607.

Kim, Y., Bertagna, F., D'Souza, E. M., Heyes, D. J., Johannissen, L. O., Sheridan, E. T., ... & Scrutton, N. S. (2021). Quantum biology: An update and perspective. *Quantum Science and Technology*, 6(2), 025005.

Kingman, J. F. C. (1982). The coalescent. *Stochastic Processes and Their Applications*, 13(3), 235–248.

Klinman, J. P., & Kohen, A. (2013). Hydrogen tunneling links protein dynamics to enzyme catalysis. *Annual Review of Biochemistry*, 82, 471–496.

Koonin, E. V. (2009). Evolution of genome architecture. *The International Journal of Biochemistry & Cell Biology*, 41(2), 298–306.

Koumandou, V. L., Wickstead, B., Ginger, M. L., van der Giezen, M., Dacks, J. B., & Field, M. C. (2013). Molecular paleontology and complexity in the last eukaryotic common ancestor. *Critical Reviews in Biochemistry and Molecular Biology*, 48(4), 373–396.

Lambert, N., Chen, Y. N., Cheng, Y. C., Li, C. M., Chen, G. Y., & Nori, F. (2013). Quantum biology. *Nature Physics*, 9(1), 10–18.

Lane, N. (2011). Energetics and genetics across the prokaryote-eukaryote divide. *Biology Direct*, 6(1), 35.

Lane, N. (2015). *The vital question: Energy, evolution, and the origins of complex life*. WW Norton.

Lane, N., & Martin, W. (2010). The energetics of genome complexity. *Nature*, 467(7318), 929–934.

Leman, L., Orgel, L., & Ghadiri, M. R. (2004). Carbonyl sulfide-mediated prebiotic formation of peptides. *Science*, 306(5694), 283–286.

Liu, Y., Makarova, K. S., Huang, W. C., Wolf, Y. I., Nikolskaya, A. N., Zhang, X., ... & Koonin, E. V. (2021). Expanded diversity of Asgard archaea and their relationships with eukaryotes. *Nature*, 593(7860), 553–557.

Löwe, J., & Amos, L. A. (2009). Evolution of cytomotive filaments: The cytoskeleton from prokaryotes to eukaryotes. *The International Journal of Biochemistry & Cell Biology*, 41(2), 349–358.

Löwdin, P. O. (1963). Proton tunneling in DNA and its biological implications. *Reviews of Modern Physics*, 35(3), 724–732.

Lynch, M. (2007). *The origins of genome architecture*. Sinauer Associates.

Lynch, M., & Conery, J. S. (2003). The origins of genome complexity. *Science*, 302(5649), 1401–1404.

Marais, A., Adams, B., Ringsmuth, A. K., Ferretti, M., Gruber, J. M., Hendrikx, R., ... & van Grondelle, R. (2018). The future of quantum biology. *Journal of the Royal Society Interface*, 15(148), 20180640.

Martijn, J., Vosseberg, J., Guy, L., Offre, P., & Ettema, T. J. (2018). Deep mitochondrial origin outside the sampled alphaproteobacteria. *Nature*, 557(7703), 101–105.

Martin, W., & Müller, M. (1998). The hydrogen hypothesis for the first eukaryote. *Nature*, 392(6671), 37–41.

Martin, W., & Russell, M. J. (2003). On the origins of cells: A hypothesis for the evolutionary transitions from abiotic geochemistry to chemoautotrophic prokaryotes, and from prokaryotes to nucleated cells. *Philosophical Transactions of the Royal Society of London. Series B: Biological Sciences*, 358(1429), 59–85.

Martin, W. F., Garg, S., & Zimorski, V. (2024). Endosymbiotic theories for eukaryote origin. *Philosophical Transactions of the Royal Society B*, 379(1892), 20220398.

McFadden, J., & Al-Khalili, J. (2018). The origins of quantum biology. *Proceedings of the Royal Society A*, 474(2220), 20180674.

Mehta, A. P., Saez-Jimenez, V., & Tsai, P. K. (2024). Engineering synthetic endosymbiosis. *Nature Chemical Biology*, 20(1), 45–53.

Miller, S. L. (1953). A production of amino acids under possible primitive Earth conditions. *Science*, 117(3046), 528–529.

Mirarab, S., & Warnow, T. (2015). ASTRAL-II: Coalescent-based species tree estimation with many hundreds of taxa and thousands of genes. *Bioinformatics*, 31(12), i44–i52.

Moody, E. R., Mahendrarajah, T. A., Dombrowski, N., Clark, J. W., Petitjean, C., Offre, P., ... & Williams, T. A. (2024). An estimate of the deepest branches of the tree of life from ancient vertically evolving genes. *eLife*, 13, e90527.

Morowitz, H. J. (1992). *Beginnings of cellular life: Metabolism recapitulates biogenesis*. Yale University Press.

Naaman, R., & Waldeck, D. H. (2012). Chiral-induced spin selectivity effect. *The Journal of Physical Chemistry Letters*, 3(16), 2178–2187.

Ohta, T. (1973). Slightly deleterious mutant substitutions in evolution. *Nature*, 246(5428), 96–98.

Ozturk, S. F., Sasselov, D. D., & Bhowmick, D. K. (2023). Origin of biological homochirality by crystallization of an RNA precursor on a magnetic surface. *Science Advances*, 9(24), eadg8274.

Pizzarello, S., & Groy, T. L. (2011). Molecular asymmetry in extraterrestrial organic chemistry: An analytical perspective. *Geochimica et Cosmochimica Acta*, 75(2), 645–656.

Plenio, M. B., & Huelga, S. F. (2008). Dephasing-assisted transport: Quantum networks and biomolecules. *New Journal of Physics*, 10(11), 113019.

Powner, M. W., Gerland, B., & Sutherland, J. D. (2009). Synthesis of activated pyrimidine ribonucleotides in prebiotically plausible conditions. *Nature*, 459(7244), 239–242.

Prigogine, I. (1977). *Self-organization in nonequilibrium systems*. Wiley.

Rajamani, S., Vlassov, A., Benner, S., Coombs, A., Olasagasti, F., & Deamer, D. (2008). Lipid-assisted synthesis of RNA-like polymers from mononucleotides. *Origins of Life and Evolution of Biospheres*, 38(1), 57–74.

Rannala, B., & Yang, Z. (2003). Bayes estimation of species divergence times and ancestral population sizes using DNA sequences from multiple loci. *Genetics*, 164(4), 1645–1656.

Ratcliff, W. C., Denison, R. F., Borrello, M., & Travisano, M. (2012). Experimental evolution of multicellularity. *Proceedings of the National Academy of Sciences*, 109(5), 1595–1600.

Ritz, T., Thalau, P., Phillips, J. B., Wiltschko, R., & Wiltschko, W. (2004). Resonance effects indicate a radical-pair mechanism for avian magnetic compass. *Nature*, 429(6988), 177–180.

Rodriguez-Garcia, M., Surman, A. J., Cooper, G. J., Suárez-Marina, I., Hosni, Z., Lee, M. P., & Cronin, L. (2015). Formation of oligopeptides in high yield under simple programmable conditions. *Nature Communications*, 6(1), 8385.

Rodrigues-Oliveira, T., Wollweber, F., Madlung, A., Kölpfer, A., Exhausted, M., & Etemad, B. (2025). Actin cytoskeleton and complex cell architecture in an Asgard archaeon. *Nature*, 627, 543–550.

Ronquist, F., Teslenko, M., Van Der Mark, P., Ayres, D. L., Darling, A., Höhna, S., ... & Huelsenbeck, J. P. (2012). MrBayes 3.2: Efficient Bayesian phylogenetic inference and model choice across a large model space. *Systematic Biology*, 61(3), 539–542.

Russell, M. J., & Martin, W. (2003). On the origins of metabolism. *Journal of Molecular Evolution*, 57(1), S1–S2.

Segré, D., & Lancet, D. (2000). Composing life. *EMBO Reports*, 1(3), 217–222.

Smith, D. R., & Keeling, P. J. (2015). Mitochondrial and plastid genome architecture: Reoccurring themes, but significant differences at the extremes. *Proceedings of the National Academy of Sciences*, 112(33), 10177–10184.

Sobron, P., Wang, A., & Mayer, J. (2020). Non-aqueous formose-like pathways in solids: Implications for early Solar System chemistry. *Icarus*, 346, 113795.

Soai, K., Shibata, T., Morioka, H., & Choji, K. (1995). Asymmetric autocatalysis and amplification of enantiomeric excess of a chiral molecule. *Nature*, 378(6559), 767–768.

Speijer, D., Lukes, J., & Eliáš, M. (2015). Sex is a ubiquitous, ancient, and inherent attribute of eukaryotic life. *Proceedings of the National Academy of Sciences*, 112(29), 8827–8834.

Sterner, R. W., & Elser, J. J. (2002). *Ecological stoichiometry: The biology of elements from molecules to the biosphere*. Princeton University Press.

Stüeken, E. E., Kipp, M. A., Koehler, M. C., & Buick, R. (2016). The evolution of Earth's biogeochemical nitrogen cycle. *Earth-Science Reviews*, 160, 220–239.

Sutherland, J. D. (2016). The origin of life—out of the blue. *Angewandte Chemie International Edition*, 55(1), 104–121.

Thiergart, T., Landan, G., Schenk, M., Dinkelaker, T., & Martin, W. F. (2012). An evolutionary network of genes present in the eukaryote common ancestor polls genomes on eukaryotic and mitochondrial origin. *Genome Biology and Evolution*, 4(4), 466–485.

Villani, G. (2005). Theoretical investigation of hydrogen transfer mechanism in the adenine-thymine base pair. *Chemical Physics*, 316(1-3), 1–8.

Vlassov, A. V., Kazakov, S. A., Johnston, B. H., & Landweber, L. F. (2005). The RNA world on ice: A new scenario for the emergence of RNA information. *Journal of Molecular Evolution*, 61(2), 264–273.

von Heijne, G. (1986). Why mitochondria need a genome. *FEBS Letters*, 198(1), 1–4.

Wächtershäuser, G. (1988). Before enzymes and templates: Theory of surface metabolism. *Microbiological Reviews*, 52(4), 452–484.

Williams, T. A., Szöllősi, G. J., Spang, A., Foster, P. G., Heaps, S. E., Boussau, B., ... & Embley, T. M. (2024). Integrative modeling of gene and genome evolution roots the archaeal tree of life. *Proceedings of the National Academy of Sciences*, 114(23), E4602–E4611.

Wochner, A., Attwater, J., Coulson, A., & Holliger, P. (2011). Ribozyme-catalyzed transcription of an active ribozyme. *Science*, 332(6026), 209–212.

Yarus, M. (2017). The genetic code and RNA-amino acid affinities. *Life*, 7(2), 13.